2014

Cold Molecular Gas in Merger Remnants. I. Formation of Molecular Gas Disks

Junko Ueda

Daisuke Iono

Min S. Yun

Alison F. Crocker

Desika Narayanan
Haverford College, dnarayan@haverford.edu

The Astrophysical Journal Supplement Series, 214:1 (29pp), 2014 September doi:10.1088/0067-0049/214/1/1

COLD MOLECULAR GAS IN MERGER REMNANTS. I. FORMATION OF MOLECULAR GAS DISKS

Junko Ueda[1,2,3], Daisuke Iono[1,4], Min S. Yun[5], Alison F. Crocker[6], Desika Narayanan[7], Shinya Komugi[1], Daniel Espada[1,4,8], Bunyo Hatsukade[1], Hiroyuki Kaneko[9], Yuichi Matsuda[1,4], Yoichi Tamura[10], David J. Wilner[3], Ryohei Kawabe[1], and Hsi-An Pan[4,11,12]

[1] National Astronomical Observatory of Japan, 2-21-1 Osawa, Mitaka,Tokyo 181-8588, Japan; junko.ueda@nao.ac.jp
[2] Department of Astronomy, School of Science, The University of Tokyo, 7-3-1 Hongo, Bunkyo-ku, Tokyo 133-0033, Japan
[3] Harvard-Smithsonian Center for Astrophysics, 60 Garden Street, Cambridge, MA 02138, USA
[4] Department of Astronomical Science, The Graduate University for Advanced Studies (SOKENDAI), 2-21-1 Osawa, Mitaka, Tokyo 181-8588, Japan
[5] Department of Astronomy, University of Massachusetts, Amherst, MA 01003, USA
[6] Ritter Astrophysical Research Center, University of Toledo, Toledo, OH 43606, USA
[7] Department of Astronomy, Haverford College, 370 Lancaster Avenue, Haverford, PA 19041, USA
[8] Joint ALMA Observatory, Alonso de Córdova 3107, Vitacura, Santiago 763-0355, Chile
[9] Graduate School of Pure and Applied Sciences, University of Tsukuba, 1-1-1 Tennodai, Tsukuba, Ibaraki 305-8577, Japan
[10] Institute of Astronomy, The University of Tokyo, 2-21-1 Osawa, Mitaka,Tokyo 181-0015, Japan
[11] Nobeyama Radio Observatory, National Astronomical Observatory of Japan, 462-2 Minamimaki, Minamisaku, Nagano 384-1305, Japan
[12] Department of Physics, Faculty of Science, Hokkaido University, Kita-ku, Sapporo 060-0810, Japan
Received 2014 June 30; accepted 2014 July 10; published 2014 August 12

ABSTRACT

We present the $\lesssim$1 kpc resolution ^{12}CO imaging study of 37 optically selected local merger remnants using new and archival interferometric maps obtained with ALMA, CARMA, the Submillimeter Array, and the Plateau de Bure Interferometer. We supplement a sub-sample with single-dish measurements obtained at the Nobeyama Radio Observatory 45 m telescope for estimating the molecular gas mass (10^{7-11} $M_{\odot}$) and evaluating the missing flux of the interferometric measurements. Among the sources with robust CO detections, we find that 80% (24/30) of the sample show kinematical signatures of rotating molecular gas disks (including nuclear rings) in their velocity fields, and the sizes of these disks vary significantly from 1.1 kpc to 9.3 kpc. The size of the molecular gas disks in 54% of the sources is more compact than the *K*-band effective radius. These small gas disks may have formed from a past gas inflow that was triggered by a dynamical instability during a potential merging event. On the other hand, the rest (46%) of the sources have gas disks that are extended relative to the stellar component, possibly forming a late-type galaxy with a central stellar bulge. Our new compilation of observational data suggests that nuclear and extended molecular gas disks are common in the final stages of mergers. This finding is consistent with recent major-merger simulations of gas-rich progenitor disks. Finally, we suggest that some of the rotation-supported turbulent disks observed at high redshifts may result from galaxies that have experienced a recent major merger.

Key words: galaxies: evolution – galaxies: formation – galaxies: interactions – galaxies: ISM – galaxies: kinematics and dynamics – radio lines: galaxies

Online-only material: color figure

1. INTRODUCTION

Galaxy interactions and mergers play important roles in the formation and evolution of galaxies, as illustrated by the increasing galaxy merger rate at higher redshifts (e.g., Lin et al. 2004; Bridge et al. 2010). Gravitational interactions between galaxies have significant effects on their morphology and physical states. The degree of these effects depends on a wide variety of parameters such as collision orbit, collision speed, and relative size. Major mergers, which can lead to significant dynamical and morphological disturbances, are strongly linked to starbursts and active galactive nuclei (AGNs; e.g., Sanders & Mirabel 1996). Since the 1970s, it has been long predicted from numerical simulations that the major merger of two disk galaxies results in the formation of a spheroid-dominated early-type galaxy (Toomre 1977; Barnes & Hernquist 1992; Naab & Burkert 2003). This classical scenario is supported by observations of the stellar structures of merger remnants that resemble elliptical galaxies (e.g., Schweizer 1982; Rothberg & Joseph 2006a) and signatures of past mergers such as shells and tidal features around elliptical galaxies (e.g., Schweizer & Seitzer 1992; Schweizer 1996).

Contrary to the classical scenario of merger evolution, recent high-resolution simulations that include more realistic gas physics have shown that not all of the major mergers will become an early-type galaxy, but some will reemerge as a disk-dominated late-type galaxy (Barnes 2002; Robertson & Bullock 2008; Hopkins et al. 2009; Xu et al. 2010). During a merger, any gas that does not lose significant angular momentum through stellar torques will survive the collision, reforming a gaseous (and subsequently a stellar) disk (Springel & Hernquist 2005), while gas that falls to the galaxy center will contribute to a nuclear starburst and subsequent formation of the spheroidal component. In galaxy mergers, the chance of disk survival during the merging event depends on orbital parameters, mass ratio, and gas mass fraction of the progenitors (Hopkins et al. 2009). The same simulations also suggest that increasing the gas mass fraction leads to a more efficient disk survival as there are fewer stars to lose angular momentum to.

In order to check this theoretical prediction and to investigate the evolution of galaxies after a merging event, we have conducted a ^{12}CO imaging study of merger remnants in the local universe using millimeter/submillimeter interferometric measurements. This paper is the first of a series on our study

of merger remnants, which includes a summary of the data and focuses on the properties of the molecular gas disk in merger remnants. The focus of the second paper is to understand the evolution of merger remnants by comparing the properties of molecular gas and stellar component with early-type galaxies (i.e., Atlas3D Project; Cappellari et al. 2011; Alatalo et al. 2013; Davis et al. 2013) and late-type galaxies (i.e., BIMA-SONG; Regan et al. 2001; Helfer et al. 2003). We will also investigate the kinematics of diffuse gas using H I line measurements in a subsequent paper.

Merger remnants are completely merged galaxies that still have tidal tails, shells, and loops, which indicate past dynamical interactions. Most previous studies on merger remnants (e.g., Lake & Dressler 1986; Shier & Fischer 1998; James et al. 1999; Genzel et al. 2001; Rothberg & Joseph 2004; Dasyra et al. 2006; Rothberg & Joseph 2006a, 2006b) focused on the stellar properties. This is because the classical scenario, in which a major merger between two disk galaxies forms a new elliptical galaxy, received higher attention. The main purpose of this study is to characterize the cold molecular disks emerging from mergers by analyzing new high-resolution interferometric CO maps for 27 optically selected merger remnants obtained using the Atacama Large Millimeter/submillimeter Array (ALMA), Combined Array for Research in Millimeter-wave Astronomy (CARMA), and Submillimeter Array (SMA). We further obtained published and archival interferometric maps from ALMA, Plateau de Bure Interferometer (PdBI), and SMA, for 10 galaxies to supplement our analysis, forming a grand sample of 37 galaxies. In addition, new Nobeyama Radio Observatory (NRO) 45 m data and published single-dish measurements from the Five College Radio Astronomical Observatory (FCRAO) 14 m, Institut de Radioastronomie and Millimétrique (IRAM) 30 m, National Radio Astronomy Observatory (NRAO) 12 m, and Swedish-ESO Submillimeter Telescope (SEST) 15 m telescopes were obtained to analyze the total molecular gas content for 32 galaxies, including six galaxies that do not overlap with the sample for interferometric observations. The low critical density of low J CO transitions enable tracing diffuse molecular gas, which is distributed in a more extended fashion compared to high J CO transitions. Thus low J CO lines are the best tracer for investigating the distribution and kinematics of diffuse molecular gas.

This paper is organized as follows. We present the properties of our merger remnant sample in Section 2, observational details and data reduction process in Section 3, and new results in Section 4. We characterize the size and the kinematics of the molecular gas by fitting a simple rotating disk model to the interferometric maps in Section 5. We summarize this paper in Section 6. All values are calculated based on a ΛCDM model with $\Omega_{\rm M} = 0.3$, $\Omega_{\Lambda} = 0.7$, and $H_0 = 73$ km s^{-1} Mpc^{-1}.

2. SAMPLE SOURCES

Our sample is drawn from the merger remnant sample studied by Rothberg & Joseph (2004, RJ04 hereafter), which is a large-scale observational study of 51 merger remnants in the local universe (<200 Mpc). The sample galaxies in RJ04 are selected solely based on optical morphology that suggests an advanced merger stage: (1) tidal tails, loops, and shells; (2) a single nucleus; and (3) absence of nearby companions, regardless of star formation or AGN activities. The stellar components in a majority of their sample have undergone violent relaxation, though seven sources show evidence for incomplete phase mixing (RJ04). Their analysis also shows the presence of "excess light" in the surface brightness profiles of nearly one-third of their sample, suggesting the effect of central starbursts.

We have obtained new and published interferometric CO maps of 37 merger remnants from this parent sample. In addition, we have obtained new and published single-dish CO measurements of 26/37 merger remnants to accurately estimate the total CO flux. We note that the exact fraction of these sources that result from a major as opposed to a minor merger is unknown since it is difficult to reverse the chronology and disentangle the exact mass and morphology of the progenitors. The K-band images (RJ04) of 37 merger remnants are presented in Figure 1 (left) and Figure 2, and the basic properties of these sources are summarized in Table 1. The K-band images show single nuclei in all of the sample sources. However a double nucleus, which suggests an incomplete merger, was found in a few sources in the radio continuum maps (e.g., NGC 3256; Norris & Forbes 1995).

We estimate the far-infrared (FIR) luminosities of our sample using the *IRAS* data at 60 μm and 100 μm (Beichman et al. 1988; Moshir et al. 1992, 2008). The FIR luminosities of our sample range from $10^9\,L_\odot$ to $10^{12}\,L_\odot$, but nine galaxies are not detected by *IRAS* and we estimate upper limits of the FIR luminosities. One galaxy (UGC 8058) is classified as an ultra-luminous infrared galaxy (ULIRG; $L_{\rm FIR} \geqslant 10^{12}\,L_\odot$), and 12 galaxies are classified as LIRGs ($L_{\rm FIR} \geqslant 10^{11}\,L_\odot$).

RJ04 estimate the Sérsic index (n) of the merger remnant from the Sérsic profile, which is a generalized form of the de Vaucouleurs profile to probe the stellar surface brightness. The Sérsic index is $n = 1$ for an exponential disk, whereas $n = 4$ for a de Vaucouleurs profile. The upper limit of the Sérsic fits is $n = 10$, thus a fit resulting in $n = 10$ may signify inaccurate fits. In our sample of 37, there are 12 galaxies with $n < 3$, 12 galaxies with $3 \leqslant n < 5$, three galaxies with $5 \leqslant n < 10$, and 10 galaxies with $n = 10$.

3. OBSERVATIONS AND ARCHIVAL DATA

3.1. Interferometric Observations with ALMA

The ^{12}CO ($J = 1$–0) observations for 20 galaxies (see Table 2) were carried out during the ALMA Cycle 0 period. All galaxies except for NGC 455 are located in the southern sky (Decl. < 0°). We used the compact configuration for the three nearby galaxies (Arp 230, AM 0956-282, and NGC 7727) and the extended configuration for the other 17 galaxies to achieve $\lesssim$1 kpc spatial resolution. The number of 12 m antennas was 16–24 depending on observation. The primary beam of the 12 m antenna is ∼50″ at 115 GHz. The correlator was configured to have four spectral windows, each with 1.875 GHz bandwidth and 488 kHz frequency resolution.

We imaged the calibrated visibility data using the Common Astronomy Software Applications package. The basic properties of the data are summarized in Table 2. The synthesized beam sizes range between 1.″2 and 4.″1 by adopting Briggs weighting of the visibilities (robust = 0.5). This weighting is recommended as it offers a good compromise between sensitivity and resolution. The achieved rms noise levels in the velocity resolution of 20 km s^{-1} are 1.78–5.26 mJy beam^{-1}. In addition, we made the continuum maps using the line free channels. The uncertainty of flux calibration is 5%.

3.2. Interferometric Observations with SMA

The ^{12}CO ($J = 2$–1) observations for five galaxies (NGC 828, UGC 2238, UGC 9829, NGC 6052, and UGC 10675) were

Table 1
Merger Remnant Sample

ID	Name	R.A. (J2000)	Decl. (J2000)	V_{sys}[a] (km s^{-1})	D_L (Mpc)	Scale (pc/1″)	log L_{FIR} ($L_\odot$)	M_K[a] (mag)	R_{eff}[b] (kpc)	Sérsic n[a]
(1)	(2)	(3)	(4)	(5)	(6)	(7)	(8)	(9)	(10)	(11)
1	UGC 6	00 03 09	21 57 37	6582	91.5	425	10.91	−24.01	0.51	10.00
2	NGC 34	00 11 06	−12 06 26	5931	82.6	385	11.41	−24.61	0.38	10.00
3	Arp 230	00 46 24	−13 26 32	1742	23.9	115	9.57	−21.75	0.69	1.56
4	NGC 455	01 15 57	05 10 43	5269	73.3	343	<9.71	−24.64	5.96	6.21
5	NGC 828	02 10 09	39 11 25	5374	74.6	349	11.29	−25.36	2.67	2.99
6	UGC 2238	02 46 17	13 05 44	6436	89.8	417	11.28	−24.58	2.13	1.46
7	NGC 1210	03 06 45	−25 42 59	3928	54.4	257	<9.15	−23.72	2.90	4.08
8	AM 0318-230	03 20 40	−22 55 53	10699	150.7	681	<10.34	−25.09	2.76	5.01
9	NGC 1614	04 33 59	−08 03 44	4778	66.1	311	11.51	−24.74	3.44	10.00
10	Arp 187	05 04 53	−10 14 51	12291	173.8	778	10.80	−25.25	6.98	4.10
11	AM 0612-373	06 13 47	−37 40 37	9734	136.5	621	<10.25	−25.65	7.00	3.44
12	UGC 4079	07 55 06	55 42 13	6108	85.1	396	10.43	−23.78	7.66	3.08
13	NGC 2623	08 38 24	25 45 17	5535	77.1	360	11.53	−24.22	2.78	10.00
14	NGC 2782	09 14 05	40 06 49	2562	35.1	168	10.44	−23.83	6.35	6.68
15	UGC 5101	09 35 51	61 21 11	11809	166.8	749	11.95	−25.50	0.25	10.00
16	AM 0956-282	09 58 46	−28 37 19	980	13.6	65	<9.12	−20.50	2.19	2.45
17	NGC 3256	10 27 51	−43 54 13	2738	37.6	179	11.51	−24.72	1.84	2.17
18	NGC 3597	11 14 42	−23 43 40	3504	48.5	230	10.88	−23.72	1.28	1.87
19	AM 1158-333	12 01 20	−33 52 36	3027	41.8	199	9.96	−22.61	1.59	3.75
20	NGC 4194	12 14 09	54 31 37	2506	34.7	166	10.81	−23.21	1.01	4.59
21	NGC 4441	12 27 20	64 48 05	2674	36.8	175	9.96	−22.98	3.69	6.83
22	UGC 8058	12 56 14	56 52 25	12642	178.6	797	12.37	−27.55	0.05	10.00
23	AM 1255-430	12 58 08	−43 19 47	9026	126.6	578	<10.18	−24.93	3.01	1.87
24	AM 1300-233	13 02 52	−23 55 18	6446	89.8	417	11.41	−24.65	14.6	4.99
25	NGC 5018	13 13 01	−19 31 05	2794	38.5	183	9.61	−25.15	4.75	4.39
26	Arp 193	13 20 35	34 08 22	7000	97.5	451	11.59	−24.40	2.98	2.74
27	AM 1419-263	14 22 06	−26 51 27	6709	93.6	434	<10.19	−24.94	5.51	4.12
28	UGC 9829	15 23 01	−01 20 50	8492	118.8	545	10.39	−24.96	8.56	2.34
29	NGC 6052	16 05 13	20 32 32	4716	65.3	307	10.88	−23.55	4.14	1.13
30	UGC 10675	17 03 15	31 27 29	10134	142.5	646	11.03	−24.80	0.50	10.00
31	AM 2038-382	20 41 13	−38 11 36	6057	84.3	393	10.37	−24.70	0.97	10.00
32	AM 2055-425	20 58 26	−42 39 00	12840	181.7	810	11.95	−25.08	2.96	2.34
33	NGC 7135	21 49 46	−34 52 35	2640	36.4	173	9.05	−23.95	27.1	10.00
34	NGC 7252	22 20 44	−24 40 42	4688	64.9	305	10.66	−24.84	2.43	3.32
35	AM 2246-490	22 49 39	−48 50 58	12884	182.1	812	11.72	−25.52	8.32	10.00
36	NGC 7585	23 18 01	−04 39 01	3447	47.7	226	<9.34	−24.98	3.55	3.53
37	NGC 7727	23 39 53	−12 17 34	1855	25.6	123	<8.80	−24.23	2.40	3.41
				Additional Sources for Single-dish Observations						
38	NGC 2655	08 55 37	78 13 23	1404	19.4	93	9.86	−23.70	1.43	3.01
39	Arp 156	10 42 38	77 29 41	10778	151.6	685	10.90	−25.81	24.2	9.64
40	NGC 3656	11 23 38	55 50 32	2869	39.7	189	10.06	−23.70	5.61	4.47
41	NGC 3921	11 51 06	55 04 43	5838	81.3	379	10.20	−25.13	1.92	5.03
42	UGC 11905	22 05 54	20 38 22	7522	105.1	485	<10.02	−24.51	2.04	5.24
43	IC 5298	23 16 00	25 33 24	8197	114.5	526	11.48	−24.92	2.77	3.93

Notes. Column 1: ID number. Column 2: source name. Columns 3 and 4: right ascension and declination. Column 5: the systemic velocity. Column 6: the luminosity distance. Column 7: the spatial scale. Column 8: the far-infrared luminosity. The luminosity is estimated using the *IRAS* catalogs. Column 9: the *K*-band magnitude. Column 10: the *K*-band effective radius. Column 11: the Sérsic index. The upper limit of the Sérsic fits is $n = 10$, thus a fit resulting in $n = 10$ may signify inaccurate fits.

[a] Reference: RJ04.

[b] The effective radius from RJ04 is corrected to account for the differences between RJ04 and this work in the assumed distances to the source.

carried out using the SMA in 2011 June and October. The data were obtained using the compact configuration. The primary beam is ∼50″ at 230 GHz. The correlator was configured to have two sidebands, each with 2 GHz bandwidth and 3.25 MHz frequency resolution.

Data inspection was carried out using the IDL-based SMA calibration tool MIR and imaging was done using the MIRIAD package. The basic properties of the data are summarized in Table 2. The synthesized beam sizes range between 2.″6 and 4.″2 by adopting natural weighting of the visibilities, which gives maximum sensitivity. The achieved rms noise levels in the velocity resolution of 20 km s^{-1} are 18.2–27.3 mJy beam^{-1}. The uncertainty of flux calibration is 20%.

3.3. Interferometric Observations with CARMA

The ^{12}CO (J = 1–0) observations for two galaxies (UGC 6 and UGC 4079) were carried out using the CARMA in 2011 January and February. The data were obtained using the C configuration. The primary beam of the 10.4 m antenna is ∼60″

Table 2
Properties of Interferometric CO Observations

ID	Name	Transition	Telescope	Spectral Res. (km s^{-1})	rms (mJy Beam^{-1})	Norm. rms (mJy Beam^{-1})	Beam Size (arcsec)	Date
(1)	(2)	(3)	(4)	(5)	(6)	(7)	(8)	(9)
1	UGC 6	CO (1–0)	CARMA	100	3.72	8.32	1.93 × 1.44	2012 Jan/Feb
3	Arp 230	CO (1–0)	ALMA	5	5.83	2.92	4.45 × 3.77	2011 Nov
4	NGC 455	CO (1–0)	ALMA	20	2.07	2.07	1.58 × 1.23	2012 Jul
5	NGC 828	CO (2–1)	SMA	25	21.8	24.4	4.23 × 3.10	2011 Oct
6	UGC 2238	CO (2–1)	SMA	25	17.7	19.8	4.25 × 2.97	2011 Oct
7	NGC 1210	CO (1–0)	ALMA	20	2.14	2.14	1.41 × 1.11	2012 Jul
8	AM 0318-230	CO (1–0)	ALMA	20	3.02	3.02	1.99 × 1.25	2012 Apr
10	Arp 187	CO (1–0)	ALMA	20	2.52	2.52	2.19 × 1.23	2012 Jul
11	AM 0612-373	CO (1–0)	ALMA	20	2.75	2.75	1.93 × 1.51	2012 Jul
12	UGC 4079	CO (1–0)	CARMA	100	2.05	5.23	1.74 × 1.53	2012 Jan/Feb
16	AM 0956-282	CO (1–0)	ALMA	5	5.71	2.86	4.21 × 2.80	2011 Nov
18	NGC 3597	CO (1–0)	ALMA	20	3.98	3.98	1.56 × 1.17	2012 Apr
19	AM 1158-333	CO (1–0)	ALMA	20	4.59	4.59	1.70 × 1.14	2012 Apr
23	AM 1255-430	CO (1–0)	ALMA	20	1.78	1.78	1.95 × 1.17	2012 Jul
24	AM 1300-233	CO (1–0)	ALMA	20	2.06	2.06	2.24 × 1.07	2012 Jul
25	NGC 5018	CO (1–0)	ALMA	20	5.26	5.26	1.98 × 1.21	2012 Apr
27	AM 1419-263	CO (1–0)	ALMA	20	1.80	1.80	1.87 × 1.11	2012 Jul
28	UGC 9829	CO (2–1)	SMA	25	24.4	27.3	4.11 × 2.82	2011 Jun
29	NGC 6052	CO (2–1)	SMA	15	21.0	18.2	3.23 × 2.63	2011 Jun
30	UGC 10675	CO (2–1)	SMA	25	18.0	20.1	3.59 × 3.04	2011 Jun
31	AM 2038-382	CO (1–0)	ALMA	20	2.98	2.98	1.47 × 1.16	2012 May
32	AM 2055-425	CO (1–0)	ALMA	20	2.34	2.34	1.35 × 1.08	2012 May
33	NGC 7135	CO (1–0)	ALMA	20	3.98	3.98	1.70 × 1.13	2012 May
34	NGC 7252	CO (1–0)	ALMA	20	3.36	3.36	1.87 × 1.16	2012 May
35	AM 2246-490	CO (1–0)	ALMA	20	2.24	2.24	1.34 × 1.17	2012 May
36	NGC 7585	CO (1–0)	ALMA	20	4.46	4.46	2.26 × 1.21	2012 May
37	NGC 7727	CO (1–0)	ALMA	5	4.36	2.18	4.10 × 3.74	2011 Nov

Notes. Column 1: ID number. Column 2: source name. Column 3: the CO transition. Column 4: telescope name. Column 5: the spectral resolution of the channel map. Column 6: the noise level in the velocity resolution shown in Col. (5). Column 7: the normalized noise level in the velocity resolution of 20 km s^{-1}. Column 8: the beam size measured in the CO map. Column 9: the observation data.

Table 3
Properties of Archival Interferometric CO Data

ID	Name	Transition	Telescope	Spectral Res. (km s^{-1})	rms (mJy Beam^{-1})	Norm. rms (mJy Beam^{-1})	Beam Size (arcsec)	Reference
(1)	(2)	(3)	(4)	(5)	(6)	(7)	(8)	(9)
2	NGC 34	CO (2–1)	SMA	25	13.8	15.4	4.13 × 3.11	Archive (PI: Z. Wang)
9	NGC 1614	CO (2–1)	SMA	40	11.2	15.8	3.67 × 3.33	Wilson et al. (2008)
13	NGC 2623	CO (2–1)	SMA	40	11.2	15.8	1.21 × 0.99	Wilson et al. (2008)
14	NGC 2782	CO (1–0)	PdBI	10	1.94	1.37	2.09 × 1.51	Hunt et al. (2008)
15	UGC 5101	CO (2–1)	SMA	40	11.9	16.8	1.20 × 0.96	Wilson et al. (2008)
17	NGC 3256	CO (1–0)	ALMA	40.64	1.29	1.84	7.57 × 5.43	Science verification
20	NGC 4194	CO (2–1)	SMA	20	6.88	6.88	1.40 × 1.30	Archive (PI: S. Aalto)
21	NGC 4441	CO (1–0)	PdBI	6.56	2.92	1.67	3.25 × 2.65	Jütte et al. (2010)
22	UGC 8058	CO (3–2)	SMA	40	20.2	28.6	0.93 × 0.72	Wilson et al. (2008)
26	Arp 193	CO (3–2)	SMA	40	26.3	37.2	2.22 × 1.98	Wilson et al. (2008)

Notes. Column 1: ID number. Column 2: source name. Column 3: the CO transition. Column 4: telescope name. Column 5: the spectral resolution of the channel map. Column 6: the noise level in the velocity resolution shown in Column 5. Column 7: the normalized noise level in the velocity resolution of 20 km s^{-1}. Column 8: the beam size measured in the CO map. Column 9: reference.

at 115 GHz. The correlator was composed of 10 bands, and each band consisted of 15 channels with 31.25 MHz frequency resolution.

Data inspection and imaging were carried out using the MIRIAD package. The synthesized beam sizes are 1.″93 × 1.″44 for UGC 6 and 1.″74 × 1.″53 for UGC 4079 by adopting natural weighting of the visibilities. The achieved rms noise levels in the velocity resolution of 100 km s^{-1} are 3.72 mJy beam^{-1} for UGC 6 and 2.05 mJy beam^{-1} for UGC 4079. The uncertainty of flux calibration is 20%.

3.4. Archival Interferometric Data

We further obtained published and archival interferometric CO maps for 10 galaxies, out of which 7 galaxies (see Table 3) were observed using the SMA (e.g., Wilson et al. 2008), 2 galaxies (NGC 2782 and NGC 4441) were observed using the PdBI (Hunt et al. 2008; Jütte et al. 2010), and 1 galaxy (NGC 3256) was observed using ALMA for science verification (SV). The basic properties of the data are summarized in Table 3. The observed CO transitions are $J = 1$–0 for three galaxies, $J = 2$–1

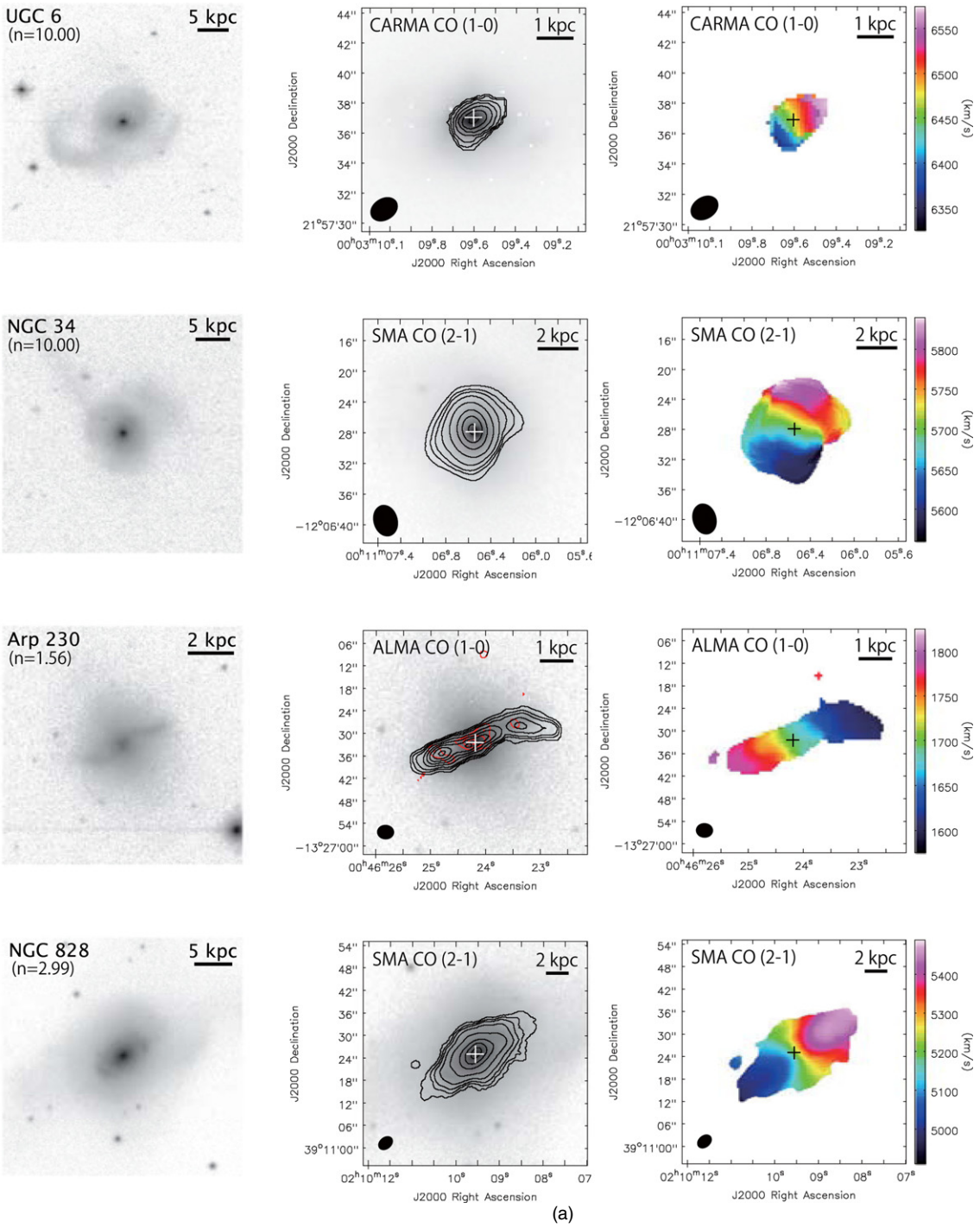

Figure 1. Left: the *K*-band images (RJ04) of UGC 6, NGC 34, Arp 230, and NGC 828. The length of each side corresponds to 90″. The magnification is selected individually for each galaxy to clearly illustrate its individual morphological structures. The number in the upper left corner is the Sérsic index estimated by Rothberg & Joseph (2004). Middle: the black contour maps of the CO integrated intensity (moment 0 maps) and red contour maps of the 3 mm continuum overlaid on the *K*-band images. The black contours are 1.2 Jy km s^{-1} × (1, 2, 3, 4, 5, 6, 7) for UGC 6, 5.6 Jy km s^{-1} × (1, 2, 3, 5, 10, 20, 30, 40) for NGC 34, 0.23 Jy km s^{-1} × (1, 2, 3, 5, 7, 9, 11, 13) for Arp 230, and 4.3 Jy km s^{-1} × (1, 2, 3, 5, 10, 20, 30, 40) for NGC 828. The red contours are 68 μJy × (3, 4, 5) for Arp 230. Right: the CO velocity fields (moment 1 maps). The moment 0 and moment 1 maps are clipped using the AIPS task, MOMNT. The plus signs in the center of the moment maps show the galactic centers defined by the *K*-band images and the ellipses in the bottom left corner of the moment maps show the beam sizes measured in the CO maps.

(A color version of this figure is available in the online journal.)

for five galaxies, and $J = 3$–2 for two galaxies. The synthesized beam sizes range between 0.″7 and 7.″6, which correspond to $\lesssim$1 kpc for each source. The achieved rms noise levels in the velocity resolution of 20 km s^{-1} are 1.37–37.2 mJy beam^{-1}. The uncertainty of flux calibration is 5% for NGC 3256, which was observed using ALMA, and 20% for the rest.

3.5. Single-dish Observations and Archival Single-dish Data

The ^{12}CO ($J = 1$–0) observations were carried out using the NRO 45 m telescope for 10 galaxies (see Table 5) during 2011 and 2012. The single-beam, two sideband, and dual-polarization receiver (T100; Nakajima et al. 2008) was used as the receiver

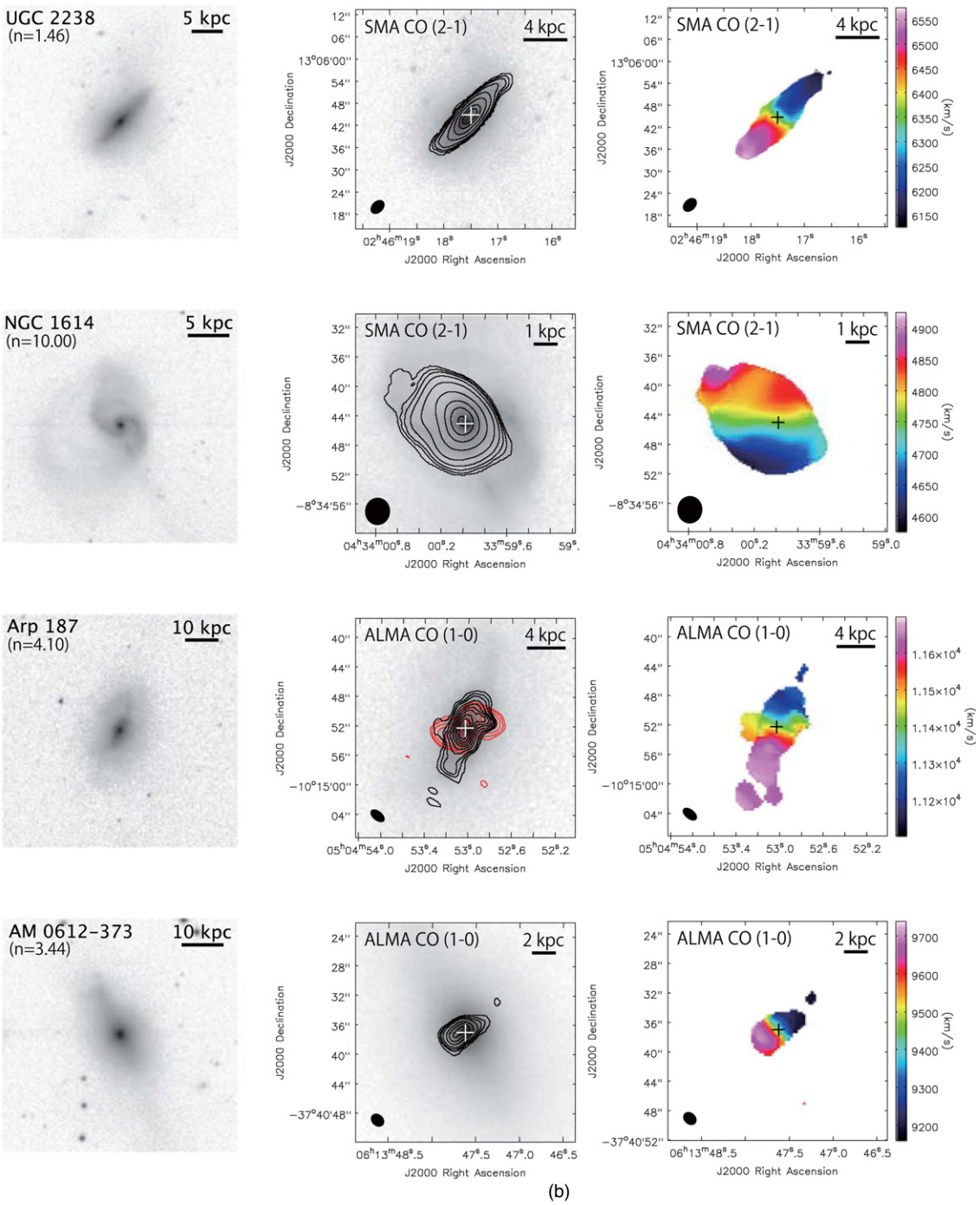

Figure 1. (Continued) Same as (a) but for UGC 2238, NGC 1614, Arp 187, and AM 0612-373. The black contours of the CO integrated intensity are 3.0 Jy km s^{-1} × (1, 2, 3, 5, 10, 20, 40, 60) for UGC 2238, 3.0 Jy km s^{-1} × (1, 2, 3, 5, 10, 25, 50, 75, 100) for NGC 1614, 0.46 Jy km s^{-1} × (1, 2, 3, 5, 7, 9, 11, 13, 15) for Arp 187, and 0.38 Jy km s^{-1} × (1, 2, 3, 5, 10, 15, 20) for AM 0612-373. The red contours of the 3 mm continuum are 110 μJy × (3, 5, 10, 20, 40, 60) for Arp 187.

front end. The analog signal from T100 is downconverted to 2–4 GHz and digitized to 3 bits before being transferred to the digital FX-type spectrometer SAM45. The 488 kHz resolution mode (2 GHz bandwidth) of SAM45 was used for the frequency resolution. Typical system temperatures were 150–200 K.

Data reduction was carried out using the AIPS-based NRO calibration tool NEWSTAR. After flagging scans with large ripples, the final spectra were made by fitting a first-order baseline. The antennae temperature (T_A^*) was converted to the main beam temperature (T_{mb}) using a main beam efficiency of $\eta_{mb} = 0.4$ and $T_{mb} = T_A^*/\eta_{mb}$. The final spectra are converted to Jansky using a Kelvin-to-Jansky conversion factor of 2.4 Jy K^{-1}. The primary beam size is ∼15″ at 115 GHz. The rms noise levels in the velocity resolution of 30 km s^{-1} range between 1 mK and 13 mK.

In addition, we gather archival single-dish CO (1–0) data for 16 galaxies. The basic properties of the archival data are summarized in Table 5. Eight galaxies were observed using the SEST 15 m telescope (Mirabel et al. 1990; Casoli et al. 1992; Huchtmeier & Tammann 1992; Andreani et al. 1995; Wiklind et al. 1995; Horellou & Booth 1997). Five galaxies were observed using the NRAO 12 m telescope (Sanders et al.

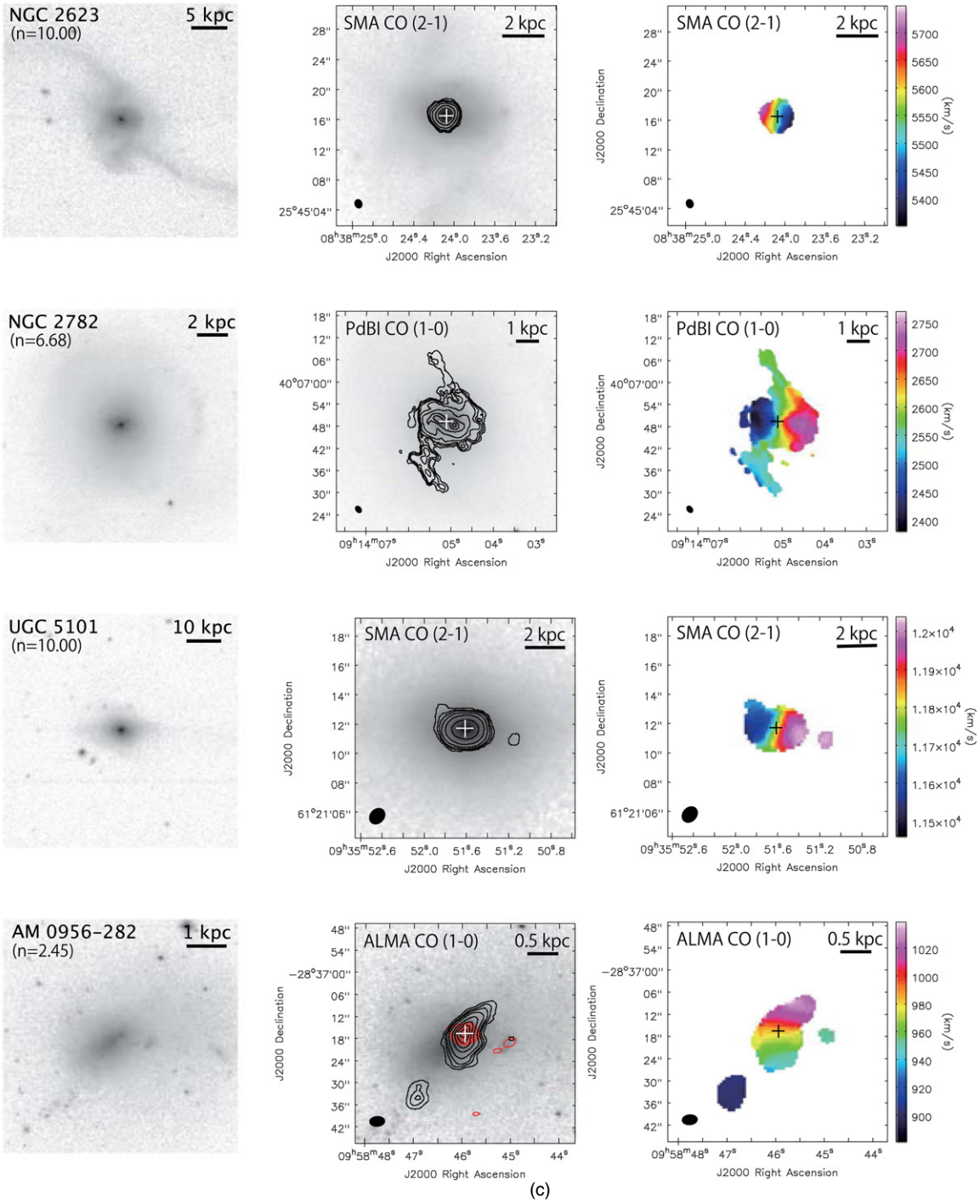

Figure 1. (Continued) Same as (a) but for NGC 2623, NGC 2782, UGC 5101, and AM 0956-282. The black contours of the CO integrated intensity are 2.0 Jy km s^{-1} × (1, 2, 3, 5, 10, 20, 30, 40) for NGC 2323, 0.19 Jy km s^{-1} × (1, 2, 3, 5, 10, 20, 30, 40) for NGC 2782, 2.3 Jy km s^{-1} × (1, 2, 3, 5, 10, 25, 50) for UGC 5101, and 0.22 Jy km s^{-1} × (1, 2, 3, 5, 10, 15, 20, 25) for AM 0956-282. The red contours of the 3 mm continuum are 60 μJy × (3, 5, 10, 15, 20, 25) for AM 0956-282.

1991; Maiolino et al. 1997; Evans et al. 2005). Two galaxies were obtained with the IRAM 30 m telescope (Zhu et al. 1999; Bertram et al. 2006), and one galaxy was obtained with the FCRAO 14 m telescope (Young et al. 1995).

4. RESULTS

4.1. Distribution and Kinematics of the CO Emission

The CO emission was newly detected in the interferometric maps of 20 out of 27 galaxies. The final number of our sample is 37 including 7 galaxies after combining with archival data. The integrated line intensities are summarized in Table 4. The integrated intensity maps and velocity fields of 30 galaxies are presented in Figure 1. They were made by smoothing and clipping the intensity using the AIPS task, MOMNT. The cleaned image cube was smoothed both spatially and in velocity and then this cube was clipped at the 1.5σ level per channel for 20 galaxies observed with ALMA (Cycle 0), 5σ level per channel for NGC 3256 because of high side-lobe levels that cannot be eliminated, and 2σ level per channel for the others.

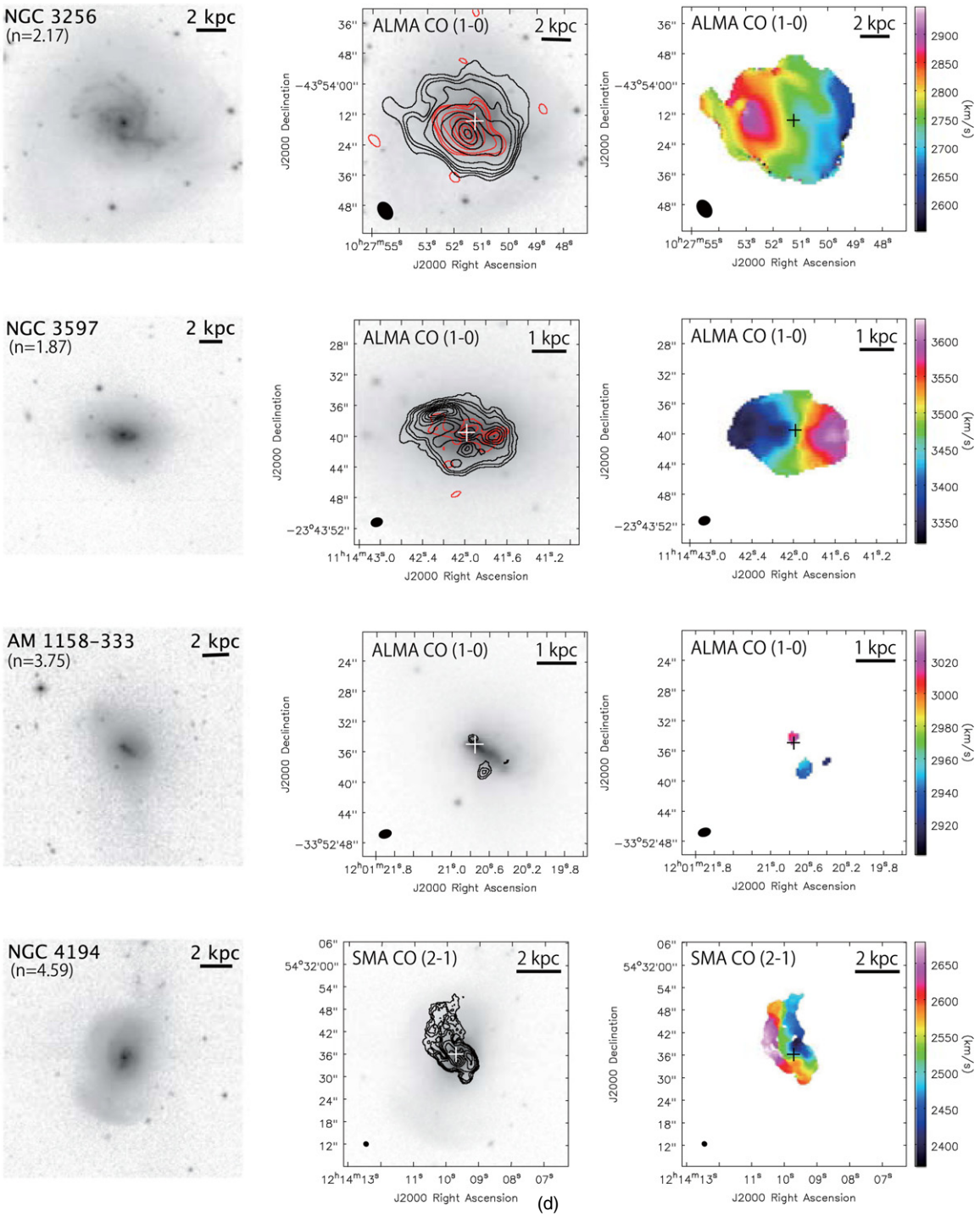

Figure 1. (Continued) Same as (a) but for NGC 3256, NGC 3597, AM 1158-333, and NGC 4194. The black contours of the CO integrated intensity are 2.0 Jy km s^{-1} × (1, 2, 3, 5, 10, 25, 50, 75, 100) for NGC 3256, 0.46 Jy km s^{-1} × (1, 2, 3, 5, 7, 9, 11, 13, 15) for NGC 3597, 0.37 Jy km s^{-1} × (1, 2, 3) for AM 1158-333, and 0.84 Jy km s^{-1} × (1, 2, 3, 5, 10, 20, 40, 60) for NGC 4194. The red contours of the 3 mm continuum are 86 μJy × (3, 5, 10, 25, 50, 75, 100, 125) for NGC 3256 and 87 μJy × (3, 5, 7, 9) for NGC 3597.

The molecular gas in 20 out of 30 galaxies detected in the CO line is distributed in the nuclear regions and the CO emission peaks roughly correspond to the peak in the *K*-band images (RJ04). In the other 10 galaxies, the CO distribution show multiple components such as arms, bars, and other structures which are not associated to the main body. Detailed description of the individual galaxies are provided in the Appendix.

Six galaxies (NGC 455, NGC 1210, AM 0318-230, UGC 4079, NGC 5018, and NGC 7585) were not detected in the CO (1–0) line. The observations of all these galaxies except for UGC 4079 have been conducted at ALMA. The 3σ upper limits of the molecular gas mass are $2 \times 10^{7-8}\,M_{\odot}$, which are estimated from the integrated intensity maps and assuming a velocity width of 300 km s^{-1}. AM 1419-263 is tentatively detected in the CO (1–0) line, but there is no robust emission ($>1.5\sigma$). Thus we classify AM 1419-263 as a non-detection because the emission is too faint to discuss the distribution and kinematics of the molecular gas. The CO (1–0) emission is not seen in

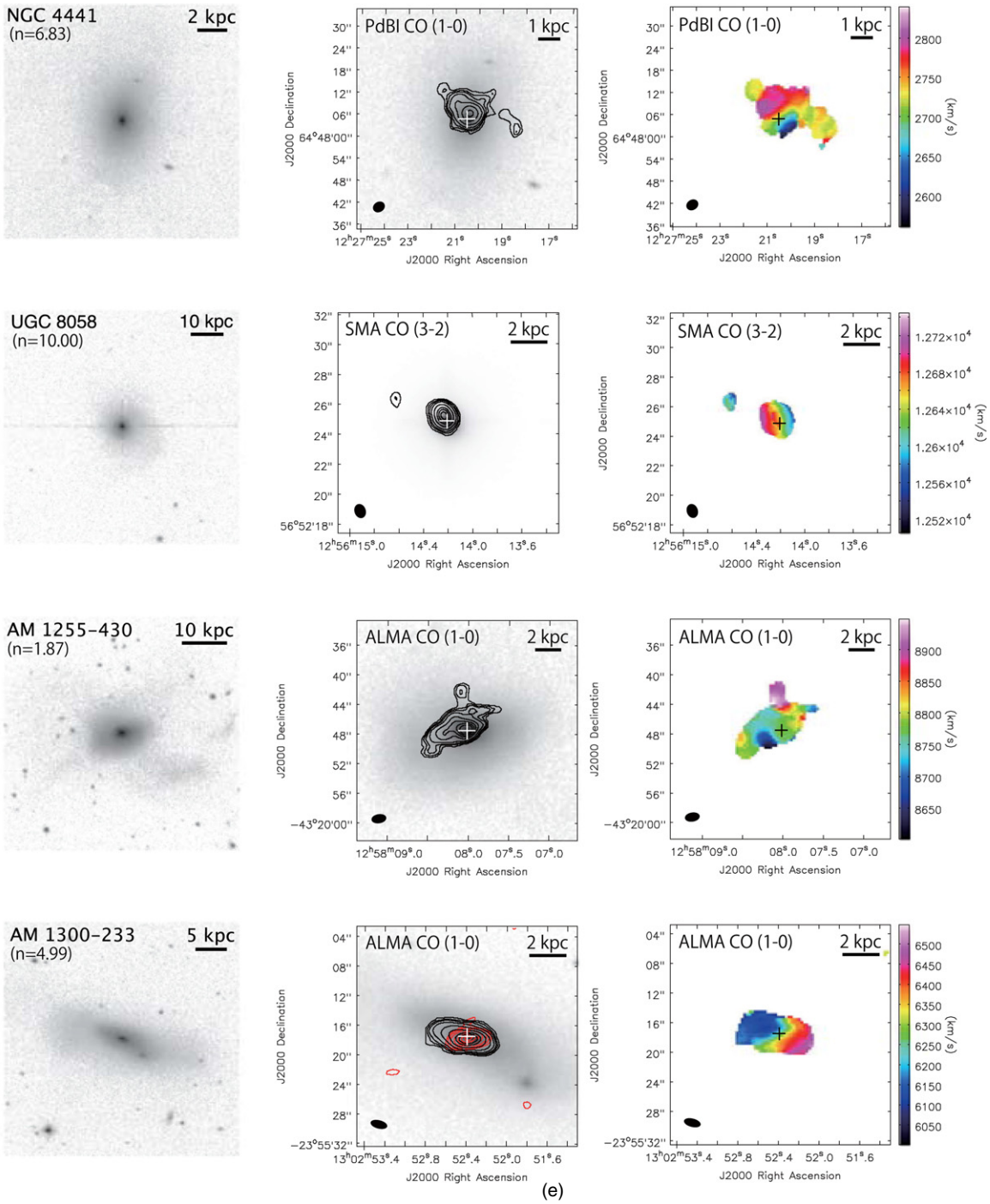

Figure 1. (Continued) Same as (a) but for NGC 4441, UGC 8058, AM 1255-430, and AM 1300-233. The black contours of the CO integrated intensity are 0.28 Jy km s^{-1} × (1, 2, 3, 5, 10, 25, 50) for NGC 4441, 5.8 Jy km s^{-1} × (1, 2, 3, 5, 10, 20, 30, 40) for UGC 8058, 0.22 Jy km s^{-1} × (1, 2, 3, 5, 10, 15, 20, 25) for AM 1255-430, and 0.39 Jy km s^{-1} × (1, 2, 3, 5, 10, 20, 40, 60) for AM 1300-233. The red contours of the 3 mm continuum are 62 μJy × (3, 5, 10, 25, 50, 75, 100) for AM 1300-233.

the interferometric map of UGC 4079 due to limited sensitivity, while the CO (1–0) spectra was clearly obtained using the single-dish measurements (Figure 3). The rms noise level in the interferometric maps is about 10 times larger than that in the single-dish spectra, assuming a beam filling factor of unity and a point source unresolved with the beam size. There are two similarities among these seven galaxies. One similarity is low FIR luminosities ($L_{\rm FIR} < 3 \times 10^{10}\,L_{\odot}$). The FIR luminosities of five galaxies are upper limits because they are not detected in the *IRAS* maps. The other is that the Sérsic indices estimated by RJ04 are distributed around $n = 4$, which suggests a de Vaucouleurs profile. The *K*-band images (RJ04) of these galaxies are presented in Figure 2. These galaxies show relatively smooth and featureless stellar spheroidal structures.

4.2. The 3 mm Continuum Maps

The 3 mm continuum emission was detected in 14 out of 21 galaxies observed using ALMA. While the CO emission was not detected in NGC 1210, NGC 5018, and AM 1419-263, the unresolved 3 mm continuum emission was clearly seen in

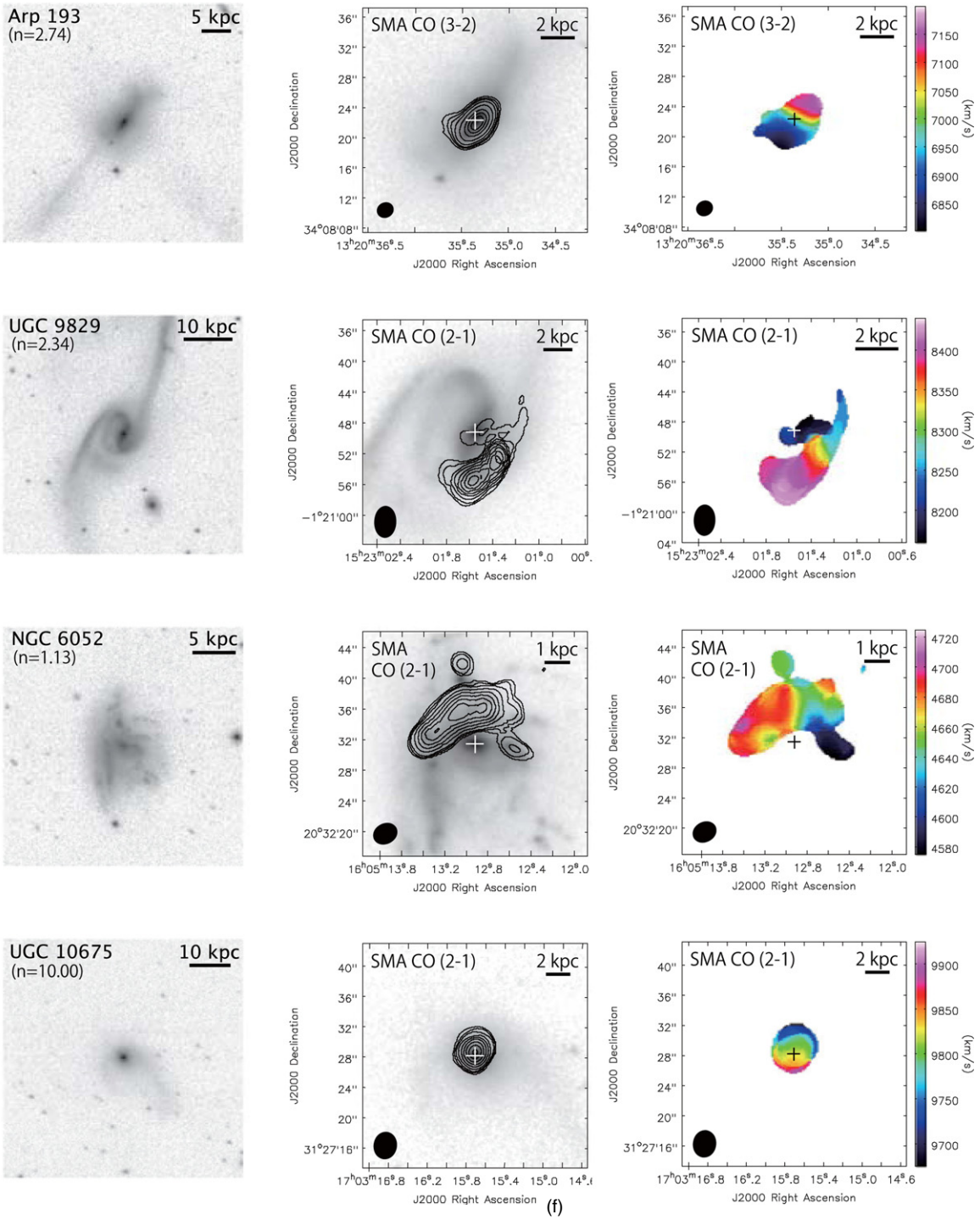

Figure 1. (Continued) Same as (a) but for Arp 193, UGC 9829, NGC 6052, and UGC 10675. The black contours of the CO integrated intensity are 10 Jy km s^{-1} × (1, 2, 3, 5, 10, 20, 30, 40) for Arp 193, 2.4 Jy km s^{-1} × (1, 2, 3, 4, 5, 6, 7, 8) for UGC 9829, 1.7 Jy km s^{-1} × (1, 2, 3, 5, 7, 9, 11, 13) for NGC 6052, and 2.4 Jy km s^{-1} × (1, 2, 3, 5, 7, 9, 11, 13, 15) for UGC 10675.

the nuclear regions. The 3 mm continuum contour maps of 11 galaxies detected in both CO (1–0) line and 3 mm continuum emission are presented in Figure 1 (middle) using red color contours. The total flux of the 3 mm continuum is summarized in Table 4 and ranges from 0.54 mJy to 27.5 mJy. The total flux was estimated by integrating the extended emission if the 3 mm continuum emission was resolved. If not, the total flux corresponds to the peak flux of the 3 mm continuum. For seven galaxies undetected in the 3 mm continuum, we estimated 3σ upper limits, assuming an unresolved point source of the nucleus. The 3σ upper limits are below 0.4 mJy. The continuum emission was unresolved in nine galaxies and associated with the nuclei defined by the *K*-band images. In the rest, the continuum emission is resolved. We remark the 3 mm continuum emission detected on the east of AM 0956-282. The peak flux is 0.24 mJy ($>3\sigma$ detection). The 3 mm continuum emission is very faint, but this is a robust detection. Detailed description of the individual galaxies are provided in the Appendix.

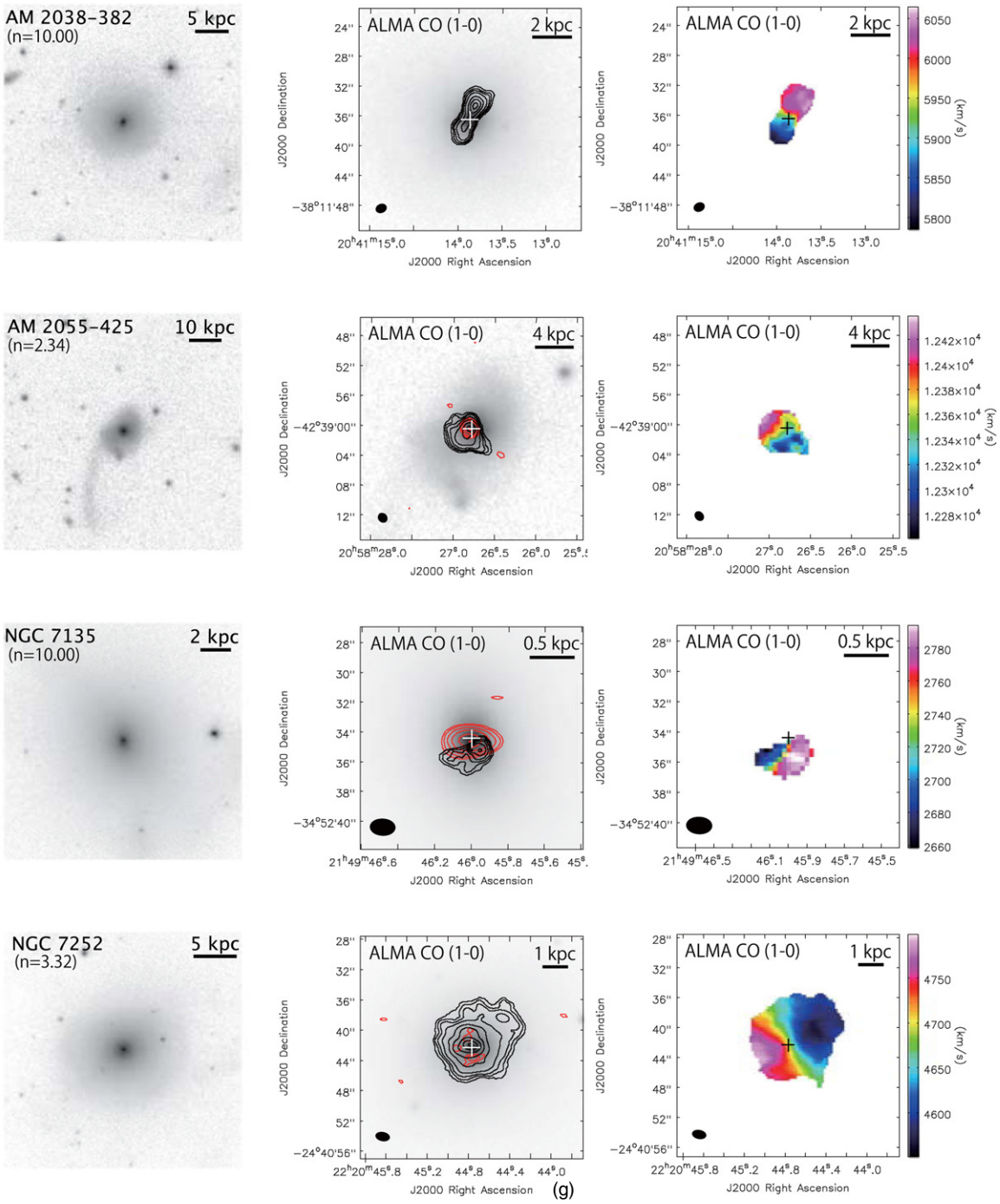

Figure 1. (Continued) Same as (a) but for AM 2038-382, AM 2055-425, NGC 7135, and NGC 7252. The black contours of the CO integrated intensity are 0.37 Jy km s^{-1} × (1, 2, 3, 5, 10, 15, 20) for AM 2038-382, 0.31 Jy km s^{-1} × (1, 2, 3, 5, 10, 25, 50) for AM 2055-425, 0.37 Jy km s^{-1} × (1, 1.5, 2, 2.5, 3, 3.5) for NGC 7135, and 0.37 Jy km s^{-1} × (1, 2, 3, 5, 10, 15, 20, 25, 30) for NGC 7252. The red contours of the 3 mm continuum are 72 μJy × (3, 5, 10, 20, 40) for AM 2055-425, 115 μJy × (3, 5, 10, 20, 40, 60) for NGC 7135, and 85 μJy × (3, 4) for NGC 7252.

4.3. Single-dish CO (1–0) Spectra and Integrated Intensity

The new CO (1–0) spectra of 16 galaxies observed using the NRO 45 m telescope are presented in Figure 3 and the properties of the data are summarized in Table 5. We report the first detections of the CO line in seven galaxies. The integrated line intensity of Arp 230 is 4.1 ± 0.8 K km s^{-1}, which corresponds to 10% of the previous measurement using the NRAO 12 m telescope (Galletta et al. 1997), the difference of which is likely attributed to the large CO extent. The integrated line intensities of NGC 2623 and NGC 2782 are 37.4 ± 7.5 K km s^{-1} and 23.5 ± 4.7 K km s^{-1}, respectively. These correspond to 53% and 25% of the previous measurements using the FCRAO 14 m telescope (Young et al. 1995). The integrated line intensities of UGC 5101, NGC 3656, NGC 4194, UGC 8058, and NGC 6052 are 17.4 ± 3.5 K km s^{-1}, 51.6 ± 10.3 K km s^{-1}, 47.7 ± 9.5 K km s^{-1}, 13.0 ± 2.6 K km s^{-1}, and 16.9 ± 3.4 K km s^{-1}, respectively. These five galaxies were observed using the IRAM 30 m telescope, and the integrated line intensities are 15.6 ± 3.1 K km s^{-1} for UGC 5101 and 22.0 ± 4.4 K km s^{-1} for UGC 8058 (Solomon et al. 1997), 23.4 K km s^{-1} for NGC 3656 (Wiklind et al. 1995), 29.26 ± 0.26 K km s^{-1} for NGC 4194

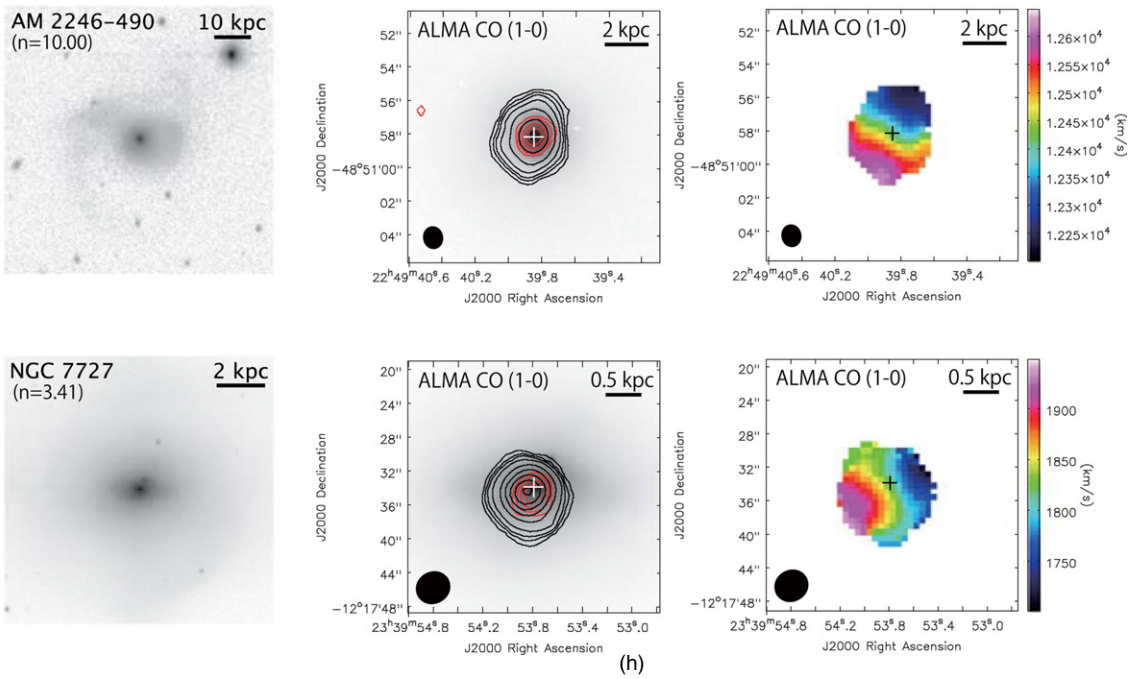

Figure 1. (Continued) Same as (a) but for AM 2246-490 and NGC 7727. The black contours of the CO integrated intensity are 0.30 Jy km s^{-1} × (1, 2, 3, 5, 10, 25, 50) for AM 2246-490 and 0.22 Jy km s^{-1} × (1, 2, 3, 5, 10, 15, 20, 25, 30) for NGC 7727. The red contours of the 3 mm continuum are 75 μJy × (3, 5, 10, 15, 20) for AM 2246-490 and 77 μJy × (3, 4, 5, 6) for NGC 7727.

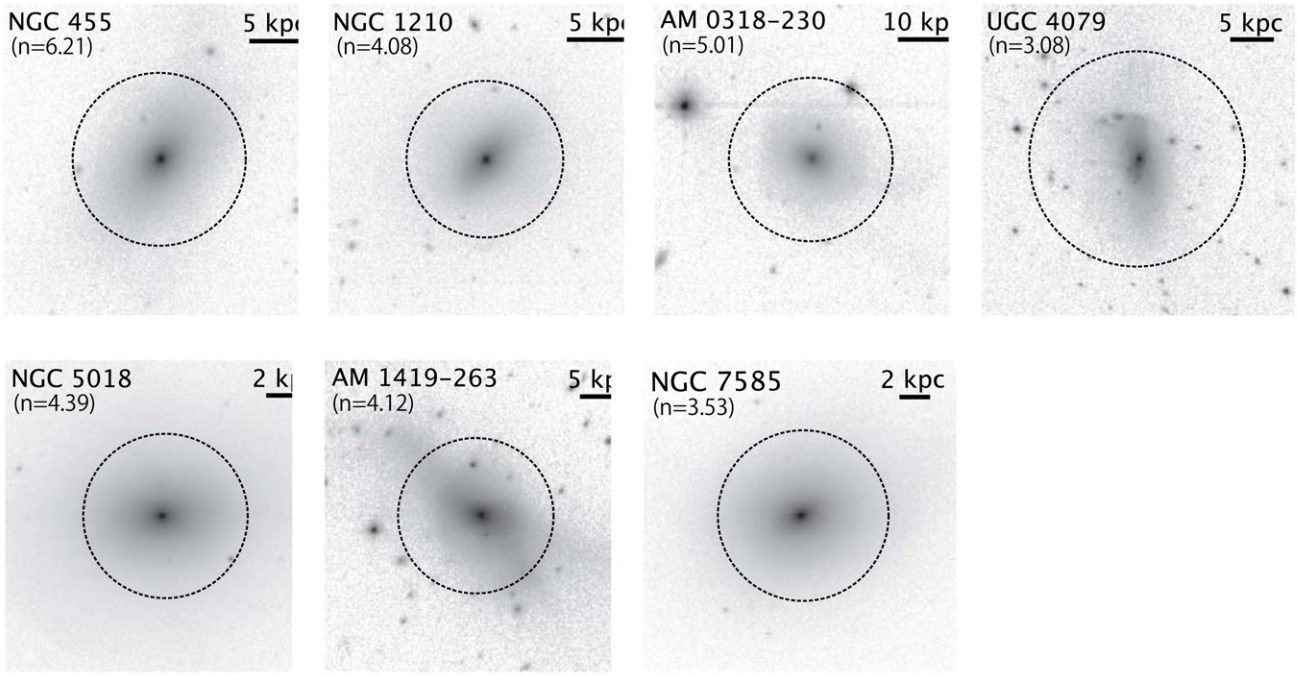

Figure 2. *K*-band images (RJ04) of seven galaxies undetected in their CO interferometric maps. The length of each side corresponds to 90″. The magnification is selected individually for each galaxy to clearly illustrate its individual morphological structures. The number in the upper left corner is the Sérsic index estimated by (RJ04). The black dotted circle shows the primary beam of interferometric observations for each galaxy. UGC 4079 is undetected in the interferometric map due to lack of sensitivity, but the CO (1–0) spectra was clearly detected using the single-dish measurements.

(Albrecht et al. 2004), and 16.4 K km s^{-1} for NGC 6052 (Albrecht et al. 2007). Using the Kelvin-to-Jansky conversion factor of 4.95 for the IRAM telescope, the ratios of the intensities of the NRO to the IRAM single-dish measurements are 60% for UGC 5101, 118% for NGC 3656, 87% for NGC 4194, 32% for UGC 8058, and 50% for NGC 6052. The ratios are quite different, which may result from multiple factors such as pointing accuracy. The total flux of NGC 4441 is 65.5 ± 13.1 Jy km s^{-1}, which is 1.6 larger than that estimated from the previous observations using the Onsala Space Observatory (OSO) 20 m telescope (Jütte et al. 2010). The total flux of the OSO single-dish measurements is estimated to be ∼40 Jy km s^{-1} from the

Table 4
The CO and 3 mm Continuum Properties

ID	Name	Transition	$S_{\nu,\mathrm{CO}}dv$ (Jy km s^{-1})	3 mm (mJy)	Recovered Flux (%)	log $M_{\mathrm{H_2,INT}}$ ($M_\odot$)
(1)	(2)	(3)	(4)	(5)	(6)	(7)
1	UGC 6	CO (1–0)	15 ± 3	...	32 (56″, 2)	9.17
2	NGC 34	CO (2–1)	386 ± 77	...	122 (11″, 3)	9.40
3	Arp 230	CO (1–0)	25 ± 1	1.88 ± 0.09	93 (15″, 1)	8.23
4	NGC 455	CO (1–0)	<0.53	<0.16	...	<7.51
5	NGC 828	CO (2–1)	1001 ± 200	...	...	9.73
6	UGC 2238	CO (2–1)	492 ± 98	...	...	9.58
7	NGC 1210	CO (1–0)	<0.50	0.54 ± 0.03	...	<7.23
8	AM 0318-230	CO (1–0)	<0.84	<0.26	...	<8.33
9	NGC 1614	CO (2–1)	722 ± 144	...	59 (22″, 3)	9.48
10	Arp 187	CO (1–0)	63 ± 3	24.3 ± 1.2	116 (57″, 4)	10.34
11	AM 0612-373	CO (1–0)	24 ± 1	<0.27	...	9.71
12	UGC 4079	CO (1–0)	<1.12	...	...	<7.97
13	NGC 2623	CO (2–1)	256 ± 51	...	...	9.16
14	NGC 2782	CO (1–0)	124 ± 25	...	54 (45″, 5)	9.24
15	UGC 5101	CO (2–1)	246 ± 49	...	71 (23″, 6)	9.81
16	AM 0956-282	CO (1–0)	25 ± 1	2.27 ± 0.11	...	7.73
17	NGC 3256	CO (1–0)	1664 ± 83	27.5 ± 1.4	80 (44″, 7)	9.66
18	NGC 3597	CO (1–0)	141 ± 7	5.78 ± 0.29	76 (44″, 8)	9.58
19	AM 1158-333	CO (1–0)	3 ± 1	<0.32	...	7.71
20	NGC 4194	CO (2–1)	84 ± 17	...	23 (12″, 3)	8.77
21	NGC 4441	CO (1–0)	43 ± 9	...	68 (15″, 1)	8.83
22	UGC 8058	CO (3–2)	392 ± 78	...	97 (23″, 9)	9.72
23	AM 1255-430	CO (1–0)	33 ± 2	<0.11	...	9.78
24	AM 1300-233	CO (1–0)	96 ± 5	8.40 ± 0.42	43 (45″, 10)	9.17
25	NGC 5018	CO (1–0)	<1.31	0.72 ± 0.04	...	<7.36
26	Arp 193	CO (3–2)	910 ± 182	...	89 (22″, 9)	9.57
27	AM 1419-263	CO (1–0)	<4.38	1.93 ± 0.10	...	<8.64
28	UGC 9829	CO (2–1)	63 ± 13	...	...	9.70
29	NGC 6052	CO (2–1)	162 ± 32	...	58 (11″, 3)	9.60
30	UGC 10675	CO (2–1)	44 ± 9	...	...	8.93
31	AM 2038-382	CO (1–0)	33 ± 2	<0.24	53 (45″, 11)	9.43
32	AM 2055-425	CO (1–0)	51 ± 3	3.85 ± 0.19	43 (46″, 10)	9.50
33	NGC 7135	CO (1–0)	4 ± 1	7.03 ± 0.35	...	7.73
34	NGC 7252	CO (1–0)	87 ± 4	1.99 ± 0.10	55 (45″, 12)	9.63
35	AM 2246-490	CO (1–0)	39 ± 2	1.91 ± 0.10	46 (46″, 10)	9.38
36	NGC 7585	CO (1–0)	<1.19	<0.28	...	<7.50
37	NGC 7727	CO (1–0)	14 ± 1	0.58 ± 0.03	...	8.02

Notes. Column 1: ID number. Column 2: source name. Column 3: the CO transition. Column 4: the CO integrated intensity. Column 5: the peak flux of the 3 mm continuum emission. Column 6: the recovered flux derived by comparing the CO flux in the same circular region using the interferometric and single-dish measurements. The diameter of the circular region and reference of the single-dish measurements are noted in brackets. Column 7: the molecular gas mass estimated using the interferometric map.
References. (1) This work; (2) Maiolino et al. 1997; (3) Albrecht et al. 2007; (4) Evans et al. 2005; (5) Young et al. 1995; (6) Papadopoulos et al. 2012b; (7) Casoli et al. 1992; (8) Wiklind et al. 1995; (9) Mao et al. 2010; (10) Mirabel et al. 1990; (11) Horellou & Booth 1997; (12) Andreani et al. 1995.

molecular gas mass reported by Jütte et al. (2010). We also use literature data of single-dish CO (1–0) measurements for 16 galaxies to discuss the molecular gas mass in a later section and the CO properties of these sources are summarized in Table 5.

We estimate the recovered flux for 18 galaxies, comparing the flux of the same CO transition in the same region measured from the interferometric maps with the single-dish spectra. For six galaxies that were observed in the CO (2–1) and CO (3–2) lines with interferometers, we obtain the CO (2–1) and CO (3–2) single-dish data from literature. The integrated line intensity I_{CO} in K km s^{-1} is converted into the integrated flux $S_{\mathrm{CO}}\Delta v$ in Jy km s^{-1} using Kelvin-to-Jansky conversion factors of 23.1 Jy K^{-1} for the FCRAO 14 m telescope, 4.95 Jy K^{-1} for the IRAM 30 m telescope, 30.4 Jy K^{-1} for the NRAO 12 m telescope, 2.4 Jy K^{-1} for the NRO 45 m telescope, and 27 Jy K^{-1} for the SEST. The recovered flux is shown in Table 4.

4.4. Molecular Gas Mass

The molecular gas mass ($M_{\mathrm{H_2}}$) is estimated from the CO integrated intensity using the following two equations (Carilli & Walter 2013; Casey et al. 2014):

$$\frac{L'_{\mathrm{CO}}}{\mathrm{K\,km\,s^{-1}}} = 3.25\times10^{7}\left(\frac{S_{\mathrm{CO}}\Delta v}{\mathrm{Jy\,km\,s^{-1}}}\right) \times\left(\frac{\nu_{\mathrm{obs}}}{\mathrm{GHz}}\right)^{-2}\left(\frac{D_{\mathrm{L}}}{\mathrm{Mpc}}\right)^{2}(1+z)^{-3}, \quad (1)$$

where L_{CO} is the CO luminosity, $S_{\mathrm{CO}}\Delta v$ is the CO integrated intensity, ν_{obs} is the observing frequency, D_L is the luminosity

Table 5
Properties of Single-dish Observations and Archival Data

ID	Name	Telescope	Beam Size (arcsec)	rms (mK)	T_{mb} (mK)	$I_{CO(1-0)}$ (K km s^{-1})	log $M_{H_2,SD}$ ($M_\odot$)	Reference
(1)	(2)	(3)	(4)	(5)	(6)	(7)	(8)	(9)
1	UGC 6	NRAO 12 m	56	...	...	1.6 ± 0.2	9.66	2
2	NGC 34	NRAO 12 m	56	...	...	3.9 ± 0.3	9.19	2
3	Arp 230	NRO 45 m	15	4.2 (20)	29.5 ± 10.6	4.1 ± 0.8	7.82	1
5	NGC 828	IRAM 30 m	22	...	...	71.1 ± 0.7	9.58	3
6	UGC 2238	NRAO 12 m	56	...	...	6.0 ± 1.2:	9.45	4
9	NGC 1614	FCRAO 14 m	46	...	...	5.8 ± 0.8	9.05	5
10	Arp 187	NRAO 12 m	57	...	...	1.8 ± 0.1	10.27	6
12	UGC 4079	NRO 45 m	15	1.2 (30)	19.7 ± 3.1	4.0 ± 0.8	8.90	1
13	NGC 2623	NRO 45 m	15	5.5 (30)	126.2 ± 13.7	37.4 ± 7.5	9.01	1
14	NGC 2782	NRO 45 m	15	7.6 (30)	121.1 ± 19.0	23.5 ± 4.7	8.91	1
15	UGC 5101	NRO 45 m	16	2.8 (30)	37.5 ± 7.1	17.4 ± 3.5	9.34	1
17	NGC 3256	SEST 15 m	44	...	...	71 ± 2	9.72	7
18	NGC 3597	SEST 15 m	44	...	...	6.9 ± 1.4	9.71	8
20	NGC 4194	NRO 45 m	15	7.7 (30)	262.6 ± 19.2	47.7 ± 9.5	9.21	1
21	NGC 4441	NRO 45 m	15	8.8 (30)	131.6 ± 21.9	22.0 ± 4.4	8.92	1
22	UGC 8058	NRO 45 m	16	3.1 (30)	60.6 ± 7.7	13.0 ± 2.6	9.27	1
24	AM 1300-233	SEST 15 m	43	...	...	8.2 ± 1.6:	9.53	9
25	NGC 5018	SEST 15 m	44	...	...	<1.4 ± 0.3:	<8.80	10
26	Arp 193	NRAO 12 m	56	...	...	7.0 ± 0.3	9.59	6
28	UGC 9829	NRO 45 m	15	1.3 (20)	46.1 ± 3.2	11.0 ± 2.2	9.63	1
29	NGC 6052	NRO 45 m	15	2.9 (10)	160.2 ± 7.1	16.9 ± 3.4	9.30	1
30	UGC 10675	IRAM 30 m	23	...	...	3.7 ± 0.2	8.99	11
31	AM 2038-382	SEST 15 m	43	...	...	2.3 ± 0.4	9.71	12
32	AM 2055-425	SEST 15 m	42	...	...	4.4 ± 0.9:	9.87	9
34	NGC 7252	SEST 15 m	43	...	...	5.8 ± 0.5	9.88	13
35	AM 2246-490	SEST 15 m	42	...	...	3.1 ± 0.6:	9.72	9
38	NGC 2655	NRO 45 m	15	6.3 (30)	53.7 ± 15.8	12.3 ± 2.5	8.11	1
39	Arp 156	NRO 45 m	15	2.9 (30)	23.5 ± 7.1	10.2 ± 2.0	9.80	1
40	NGC 3656	NRO 45 m	15	12.5 (30)	165.5 ± 31.2	51.6 ± 10.3	9.36	1
41	NGC 3921	NRO 45 m	15	1.0 (40)	25.7 ± 2.6	7.7 ± 1.5	9.30	1
42	UGC 11905	NRO 45 m	15	3.8 (30)	21.7 ± 9.5	10.1 ± 2.0	9.49	1
43	IC 5298	NRO 45 m	15	5.4 (30)	48.0 ± 13.5	11.3 ± 2.3	8.83	1

Notes. Column 1: ID number. Column 2: source name. Column 3: telescope. Column 4: the noise level in the velocity resolution shown in (). Column 5: the main beam temperature corrected for atmospheric attenuation. Column 6: the CO (1–0) line integrated intensity. Double colon means that the flux error is unknown. The error is assumed to be 20% in this paper. Column 8: the molecular gas mass estimated using the single-dish spectra. Column 7: reference.
References. (1) This work; (2) Maiolino et al. 1997; (3) Bertram et al. 2006; (4) Sanders et al. 1991; (5) Young et al. 1995; (6) Evans et al. 2005; (7) Casoli et al. 1992; (8) Wiklind et al. 1995; (9) Mirabel et al. 1990; (10) Huchtmeier & Tammann 1992; (11) Zhu et al. 1999; (12) Horellou & Booth 1997; (13) Andreani et al. 1995.

distance, and z is the redshift. Then the molecular gas mass is derived by

$$\frac{M_{H_2}}{M_\odot} = \alpha_{CO} \frac{L_{CO}}{L_\odot}, \quad (2)$$

where α_{CO} is the CO luminosity-to-H_2 mass conversion factor in $M_\odot$ pc^{-2} (K km s^{-1})$^{-1}$. The conversion factor has been a controversial issue for a long time. Solomon & Barrett (1991) find that the conversion factor is roughly constant in the Galaxy and nearby spiral galaxies and suggest that the conversion factor is $X_{CO} = 2.2 \times 10^{20}$ cm^{-2} (K km s^{-1})$^{-1}$, corresponding to $\alpha_{CO} = 4.8\ M_\odot$ pc^{-2} (K km s^{-1})$^{-1}$. However, the conversion factor in gas-rich galaxies at high redshift and local U/LIRGs is lower than the standard value in the Galaxy (e.g., $\alpha_{CO} \sim$ 0.6–0.8; Downes & Solomon 1998; Papadopoulos et al. 2012a). It is suggested that the conversion factor in mergers, on average, are lower values than those in high-redshift disk galaxies which may have gravitationally unstable clumps (Narayanan et al. 2012). Indeed, the low α_{CO} values are found in mergers such as the Antennae galaxies ($\alpha_{CO} \sim$ 0.2–1; Zhu et al. 2003) and Arp 299 ($\alpha_{CO} \sim$ 0.2–0.6; Sliwa et al. 2012).

We estimate the molecular gas mass of a merger remnant with a FIR luminosity less than $10^{11}\ L_\odot$ using the conversion factor of $\alpha_{CO} = 4.8$ (Solomon & Barrett 1991), and we use $\alpha_{CO} = 0.8$ (Downes & Solomon 1998) for the 14 U/LIRGs. In estimating the molecular gas mass from the CO (3–2) and the CO (2–1) luminosities, we convert the high-J CO luminosity into the CO (1–0) luminosity, assuming that the CO (3–2)/CO (1–0) and the CO (2–1)/CO (1–0) brightness temperature ratio is 0.5, which is similar to the average CO (3–2)/CO (1–0) ratio in local U/LIRGs estimated by Iono et al. (2009). We estimate the molecular gas mass using the single-dish CO data ($M_{H_2,SD}$) and also using the interferometric CO maps ($M_{H_2,INT}$), and summarize $M_{H_2,SD}$ and $M_{H_2,INT}$ in Table 4 and Table 5, respectively. The molecular gas mass in the sample of merger remnants ranges between $10^7\ M_\odot$ and $10^{11}\ M_\odot$.

Although $M_{H_2,SD}$ should in general be larger than $M_{H_2,INT}$ as it retrieves extended flux that is not recovered by the interferometer, some sources in Tables 4 and 5 have $M_{H_2,INT}$ that is larger than the single-dish flux. Several factors may contribute to this, such as the uncertainty in calibration, and

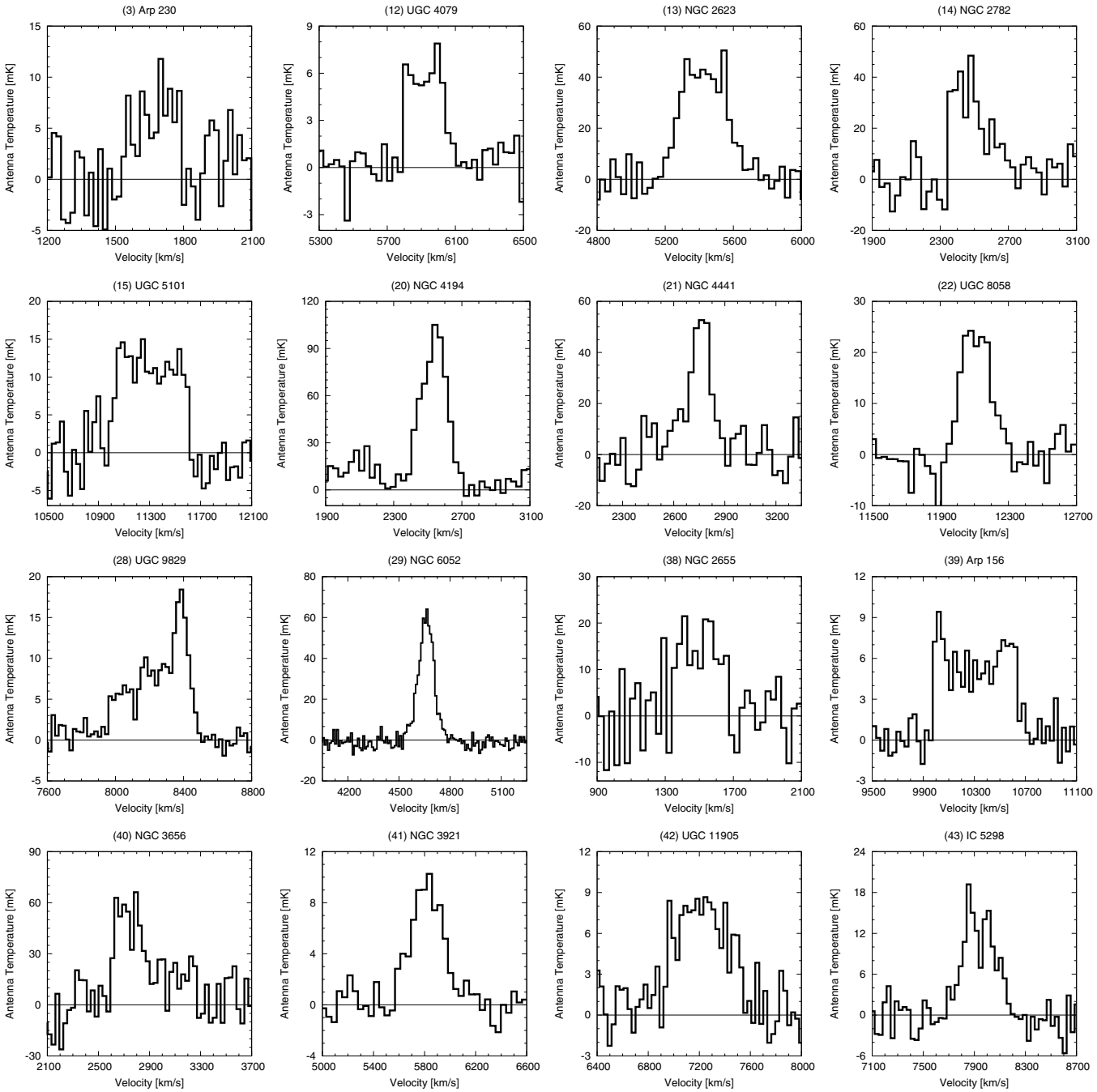

Figure 3. CO (1–0) spectra of 16 sources obtained with the NRO 45 m telescope. The primary beam size is about 15″ at 115 GHz. The velocity resolution is different for each galaxy.

possibilities that the single-dish beam did not cover all of the CO distribution for extended sources. The most likely explanation is the assumption of our CO line ratio where we use CO (3–2) or CO (2–1) for interferometric data, and CO (1–0) for single dish. We use a uniform line ratio for all sources, but there is an uncertainty in this assumed line ratio because the line ratios vary among the sources (e.g., Iono et al. 2009) due to the different physical conditions in the interstellar matter. We note, however, that the uncertainty in the relative mass between that obtained from interferometric and single-dish data does not affect the results presented in this paper. A full discussion of the molecular mass will be provided in a forthcoming paper (J. Ueda et al., in preparation; Paper II).

5. FORMATION OF THE MOLECULAR GAS DISK

In this section, we characterize the size and the kinematics of the molecular gas by fitting a simple rotating disk model to the interferometric maps. The main motivation for this work is to evaluate the size and the frequency of the occurrence of molecular disks and to investigate this in the context of recent numerical simulations that suggest the formation of an extended gas disk as a final product of a major merger (Springel & Hernquist 2005). We further estimate the relative size of the molecular gas distribution to the stellar component traced in *K*-band emission. Finally, we end this subsection with an implication to high-redshift galaxies.

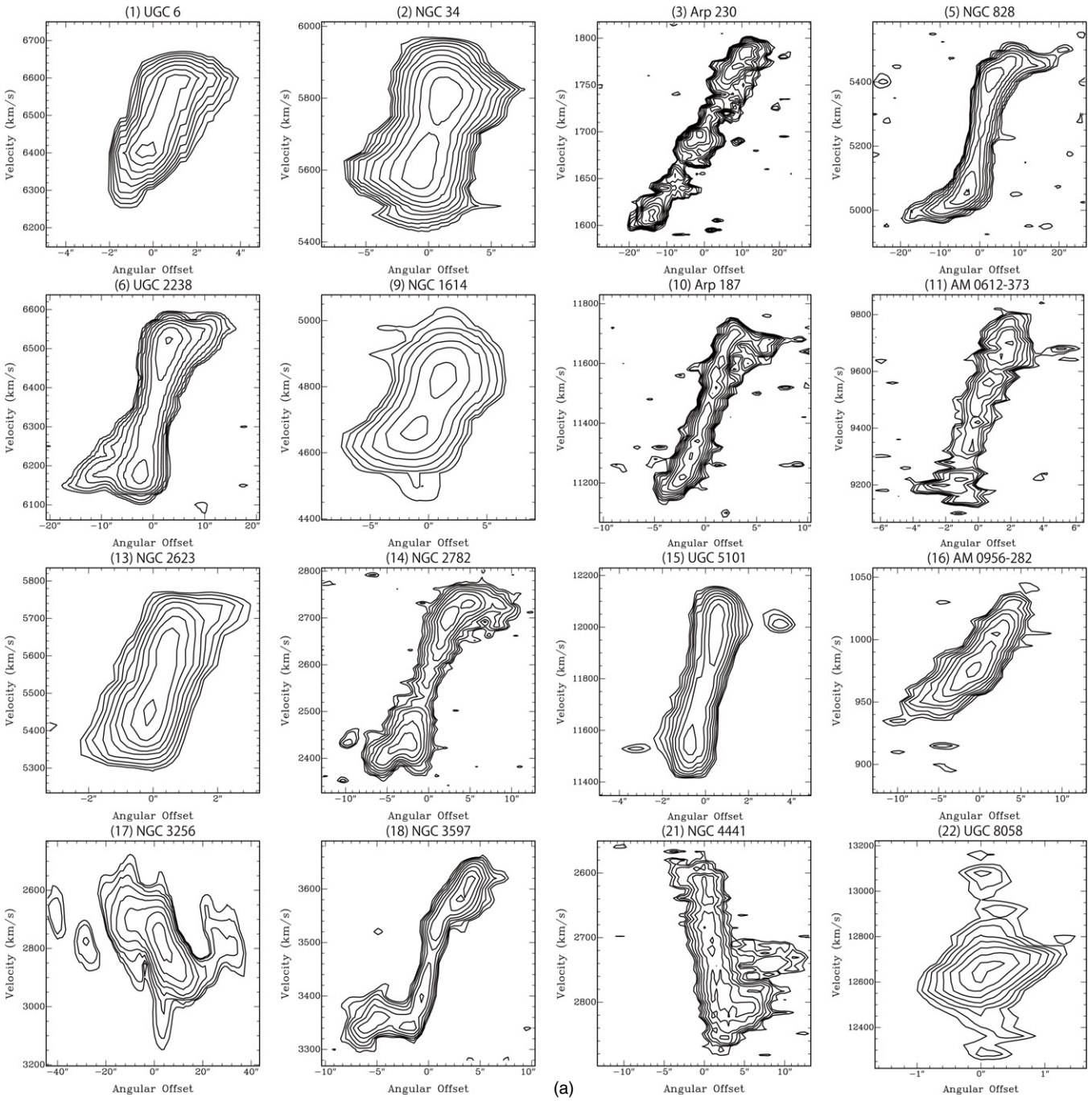

Figure 4. (a) Position–velocity diagrams along the kinematical major axes of 24 galaxies with molecular gas disks. The nth contours are defined by cp^n Jy beam^{-1}, where c is the 5σ and 2σ level for NGC3256 and other sources, respectively. The parameters are $(c, p) = (7.44, 1.2)$, (27.6, 1.4), (11.7, 1.2), (43.6, 1.5), (35.4, 1.5), (22.4, 1.9), (5.04, 1.3), (5.50, 1.3), (22.4, 1.4), (3.88, 1.5), (23.8, 1.4), (11.4, 1.4), (6.45, 2.0), (7.96, 1.4), (5.84, 1.4), and (40.4, 1.5), respectively, from top left to bottom right.

5.1. Molecular Gas Disks in Merger Remnants

It is clear from Figure 1 that most of the merger remnants show disk-like rotation in their CO velocity fields. In order to quantify the kinematics and the geometry of the rotating molecular gas, we apply a fitting program (AIPS's task GAL) to the CO velocity fields of the 30 galaxies detected in the CO line. The galactic center is defined by the emission peak of the *K*-band image (RJ04), and we assume that the molecular gas rotates around the galactic center. We fit tilted concentric ring models to the velocity field using least-squares fitting routine for the kinematical parameters and a default convergence condition.

The estimated position angle, inclination, and systemic velocity are summarized in Table 6. The fitting routine converged for 24 out of the 30 galaxies. The fitting procedure failed for the remaining six galaxies (AM 1158-333, NGC 4194, AM 1255-430, UGC 9829, NGC 6052, and NGC 7135) due to the clumpy CO distribution or the complex velocity distribution that is not characterized by a simple gas disk model. The CO distribution is strongly distorted in these six galaxies, and the CO emission is not associated with the galactic center in NGC 6052 and NGC 7135.

In addition, we investigate the position–velocity (PV) diagrams along the kinematical major axes of 24 galaxies with

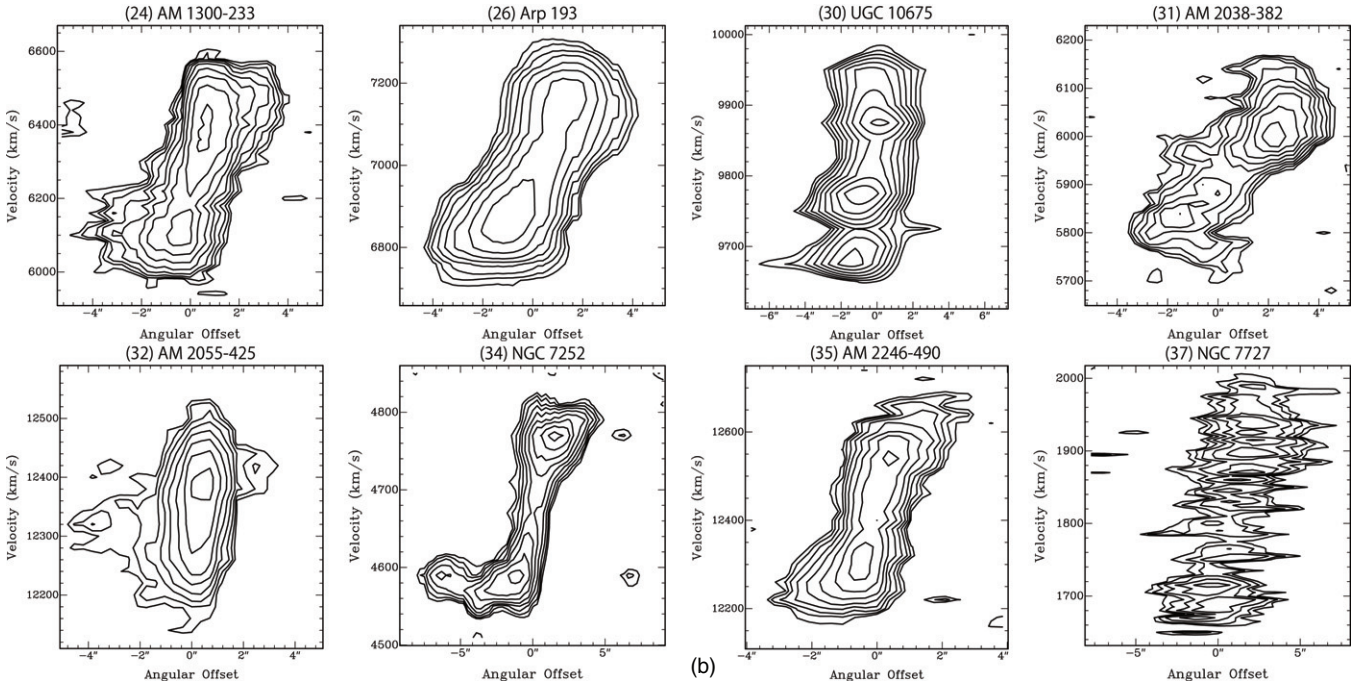

Figure 4. (Continued) (b) Same as (a). The nth contours are defined by cp^n Jy beam^{-1}, where c is the 2σ level. The parameters are $(c, p) = (4.12, 1.5)$, (52.6, 1.6), (36.0, 1.2), (5.96, 1.3), (4.68, 1.5), (6.72, 1.4), (4.48, 1.4), and (8.72, 1.4), respectively, from top left to bottom right.

molecular gas disks (Figure 4). The kinematical major axes are estimated by fitting the CO velocity fields. The PV diagrams reveal that the emission peaks are clearly shifted from the galactic centers in 18/24 galaxies (see Table 6), suggesting the presence of a ring and/or a bar. The PV diagrams of NGC 828, UGC 2238, and NGC 7252 show a double peak located at the transition point between rigid rotation and flat rotation, which may signify a spiral and/or a bar structure rather than a ring structure.

5.2. The Extent of the Molecular Gas

In order to quantify the extent of the molecular gas disk, we estimate two types of radii ($R_{\rm CO}$ and R_{80}) using the integrated intensity maps. $R_{\rm CO}$ is the radius from the galactic center that encloses the maximum extent of the molecular gas disk, and R_{80} is the radius from the galactic center, which contains 80% of the total CO flux. We chose this method because most of our attempts to fit an exponential disk were unsuccessful. In particular, the radial profiles of molecular gas deviate from an exponential profile in the outer regions. For the 24 galaxies with robust disk models in Section 5.1, we take into account the derived position angle and the inclination of the gas disk (Table 6). We define these 24 galaxies as "Type A." For six galaxies in which the CO velocity field cannot be modeled by circular motion, we define them as "Type B" and estimate $R_{\rm CO}$ and R_{80} without correcting for the geometry of the galaxy. The $R_{\rm CO}$ and R_{80} of 30 galaxies are summarized in Table 6. The histogram of $R_{\rm CO}$ is shown in Figure 5 (left). The dark and light gray bars show Type A and Type B, respectively. For three galaxies (NGC 2782, NGC 3256, and NGC 4441), we exclude the CO extensions which clearly exist outside the molecular gas disk (see Figure 1).

The histogram of R_{80} is shown in Figure 5 (right). The representation of the color is the same as in Figure 5 (left). In order to examine the effect of the detection limit on the estimated radii, we investigate the relation between 1σ mass sensitivity and R_{80}. The absence of an obvious systematic correlation allows us to argue that the detection limit does not strongly affect the observed size of the molecular gas. In addition, there is no significant effect of the different low J rotational transitions ($J =$ 1–0, 2–1, 3–2) on the estimated radii, because the distributions of the CO (1–0), CO (2–1), and CO (3–2) are not different in local galaxies such as M51 (Vlahakis et al. 2013), although the distribution may vary in different population of galaxies with extreme CO excitation conditions. The average $R_{\rm CO}$ of Type A galaxies is 3.5 ± 2.3 kpc and the average R_{80} of the molecular gas disks is 1.5 ± 0.8 kpc. Arp 187 has a molecular gas disk with the largest R_{80} of 3.5 ± 0.3 kpc. Its maximum extent is also the largest in our sample. On the other hand, AM 0956-282 has a molecular gas disk with the smallest R_{80} of 0.4 ± 0.1 kpc. The $R_{\rm CO}$ of AM 0956-282 is smaller than the average, but it is not the smallest in our sample. We estimate $R_{80,\rm MW}$ of the molecular gas disk in the Milky Way using the radially averaged surface brightness (Nakanishi & Sofue 2006). As a result, we find that $R_{80,\rm MW}$ is 8.5 ± 0.5 kpc, which is about five times larger than the average R_{80} in our sample. There is no merger remnant in the present sample, which has a less concentrated molecular gas disk than the gas disk in the Milky Way.

5.3. Comparison of the Sizes of the Molecular Gas Disk with the Stellar Component

We estimate the ratio of R_{80} to the K-band effective radius ($R_{\rm eff}$; Table 1) for our sample of merger remnants to investigate the relative size of the molecular gas disk to the stellar component. $R_{\rm eff}$ is the radius of the isophote containing half of the total K-band luminosity. The ratio between R_{80} and $R_{\rm eff}$ ($R_{\rm ratio}$, hereafter) is summarized in Table 6. The histogram of $R_{\rm ratio}$ of the 29 sources except for UGC 8058 is shown in Figure 6. The $R_{\rm ratio}$ of UGC 8058 is extremely large ($R_{\rm ratio} = 16$). UGC 8058 is the most distant source ($D_{\rm L} \simeq 180$ Mpc) in our sample, and the CO distribution is only marginally resolved and R_{80} is likely overestimated due to the large beam, leading to an

Table 6
Properties of the Molecular Gas Disk

ID	Name	Position Angle (deg)	Inclination (deg)	V_0 (km s^{-1})	R_{CO} (kpc)	R_{80} (kpc)	$\frac{R_{80}}{R_{eff}}$	Ring
(1)	(2)	(3)	(4)	(5)	(6)	(7)	(8)	(9)
1	UGC 6	306 ± 1	21 ± 9	6473 ± 1	1.2 ± 0.2	0.5 ± 0.2	1.1 ± 0.4	Y
2	NGC 34	346 ± 1	26 ± 1	5701 ± 1	3.1 ± 0.3	1.7 ± 0.3	4.5 ± 0.9	Y
3	Arp 230	113 ± 1	65 ± 1	1694 ± 1	3.2 ± 0.1	1.8 ± 0.1	2.6 ± 0.2	Y
5	NGC 828	306 ± 1	60 ± 1	5229 ± 1	7.9 ± 0.3	3.5 ± 0.3	1.3 ± 0.1	Y
6	UGC 2238	138 ± 1	61 ± 1	6361 ± 1	8.5 ± 0.4	2.6 ± 0.4	1.2 ± 0.2	Y
9	NGC 1614	352 ± 1	36 ± 1	4744 ± 1	4.6 ± 0.3	1.4 ± 0.3	0.40 ± 0.08	Y
10	Arp 187	165 ± 2	53 ± 5	11441 ± 4	9.3 ± 0.3	3.5 ± 0.3	0.50 ± 0.05	N
11	AM 0612-373	123 ± 1	45 ± 1	9465 ± 1	5.0 ± 0.3	1.3 ± 0.3	0.19 ± 0.04	Y
13	NGC 2623	76 ± 1	18 ± 4	5532 ± 1	1.1 ± 0.1	0.5 ± 0.1	0.18 ± 0.04	Y
14	NGC 2782	260 ± 1	35 ± 1	2573 ± 1	2.3 ± 0.1[a]	1.1 ± 0.1[a]	0.18 ± 0.01	Y
15	UGC 5101	256 ± 1	25 ± 2	11799 ± 6	3.0 ± 0.2	1.0 ± 0.2	4.0 ± 0.8	Y
16	AM 0956-282	353 ± 2	34 ± 7	986 ± 1	1.6 ± 0.1	0.4 ± 0.1	0.18 ± 0.03	N
17	NGC 3256	84 ± 1	43 ± 1	2760 ± 1	6.6 ± 0.3[a]	3.2 ± 0.3[a]	1.7 ± 0.2	N
18	NGC 3597	264 ± 1	55 ± 1	3475 ± 1	2.3 ± 0.1	1.5 ± 0.1	1.2 ± 0.1	Y
19	AM 1158-333	...	...	...	1.0 ± 0.1[b]	0.8 ± 0.1[b]	0.48 ± 0.04	...
20	NGC 4194	...	...	...	2.2 ± 0.1[b]	1.3 ± 0.1[b]	1.3 ± 0.1	...
21	NGC 4441	30 ± 1	31 ± 3	2716 ± 1	2.2 ± 0.1[a]	0.9 ± 0.1[a]	0.24 ± 0.03	Y
22	UGC 8058	98 ± 1	17 ± 9	12641 ± 5	1.5 ± 0.2	0.8 ± 0.2	16 ± 3	N
23	AM 1255-430	...	...	...	3.7 ± 0.2[b]	2.0 ± 0.2[b]	0.66 ± 0.07	N
24	AM 1300-233	233 ± 1	23 ± 3	6298 ± 1	2.4 ± 0.2	1.1 ± 0.2	0.08 ± 0.01	Y
26	Arp 193	331 ± 1	26 ± 2	6993 ± 1	2.6 ± 0.2	1.2 ± 0.2	0.40 ± 0.08	Y
28	UGC 9829	...	...	...	5.1 ± 0.5[b]	4.2 ± 0.5[b]	0.49 ± 0.05	...
29	NGC 6052	...	...	...	3.8 ± 0.2[b]	2.0 ± 0.2[b]	0.49 ± 0.05	...
30	UGC 10675	175 ± 1	31 ± 4	9810 ± 1	2.6 ± 0.5	1.6 ± 0.5	3 ± 1	Y
31	AM 2038-382	330 ± 1	23 ± 5	5935 ± 1	2.2 ± 0.1	1.2 ± 0.1	1.2 ± 0.1	Y
32	AM 2055-425	41 ± 2	24 ± 10	12357 ± 7	3.6 ± 0.2	1.7 ± 0.2	0.57 ± 0.08	N
33	NGC 7135	...	...	...	0.4 ± 0.1[b]	0.3 ± 0.1[b]	0.01 ± 0.01	...
34	NGC 7252	118 ± 1	23 ± 3	4684 ± 1	2.6 ± 0.1	1.5 ± 0.1	0.60 ± 0.05	Y
35	AM 2246-490	156 ± 1	30 ± 3	12439 ± 8	2.8 ± 0.3	1.3 ± 0.3	0.15 ± 0.03	Y
37	NGC 7727	113 ± 1	62 ± 2	1815 ± 1	1.6 ± 0.1	0.8 ± 0.1	0.35 ± 0.05	N

Notes. Column 1: ID number. Column 2: source name. Columns 3–5: the position angle, inclination, and systemic velocity of the molecular gas disk. These parameters are estimated by fitting the CO velocity field. Column 6: the radius enclosing the maximum extent of the molecular gas disk and the CO distribution. Column 7: the radius enclosing 80% of the total CO flux. Column 8: the ratio of R_{80} to the K-band effective radius (R_{eff}; RJ04). Column 9: "Y" means that a ring-like structure is seen in the PV diagram along the kinematical major axis.
[a] The radii are estimated after excluding the CO extensions which clearly exist outside the molecular gas disk.
[b] The radii are estimated without correcting for the geometry of the galaxy.

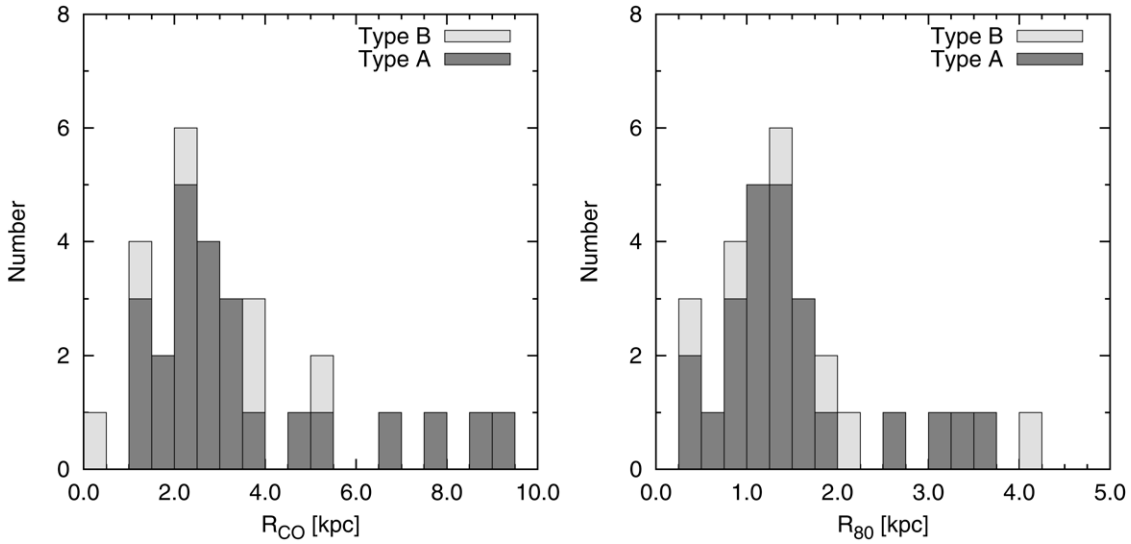

Figure 5. Histogram of the molecular gas extent. R_{CO} is the maximum size of the molecular gas extent (left) and R_{80} is the radius that contains 80% of the total CO flux (right). The dark gray bars show the number of sources with the molecular gas disk (Type A). The light gray bars show the number of sources in which the CO velocity field cannot be modeled by circular motion (Type B).

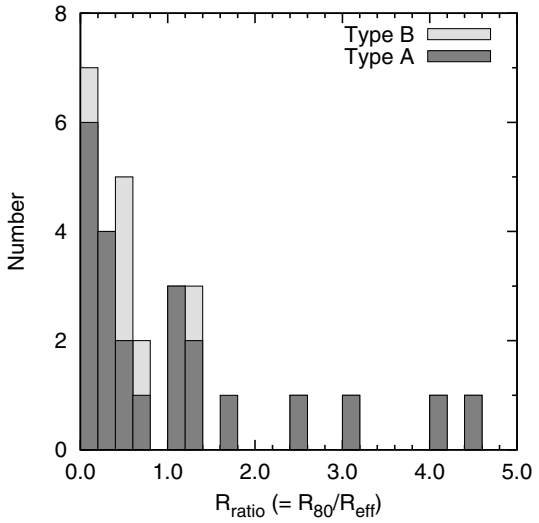

Figure 6. Histogram of the relative size of the molecular gas extent to the stellar component in 29 merger remnants. R_{80} is the radius which contains 80% of the total CO flux and $R_{\rm eff}$ is the radius of the isophote containing half of the total K-band luminosity. The dark gray and light gray bars show the number of Type A and Type B, respectively.

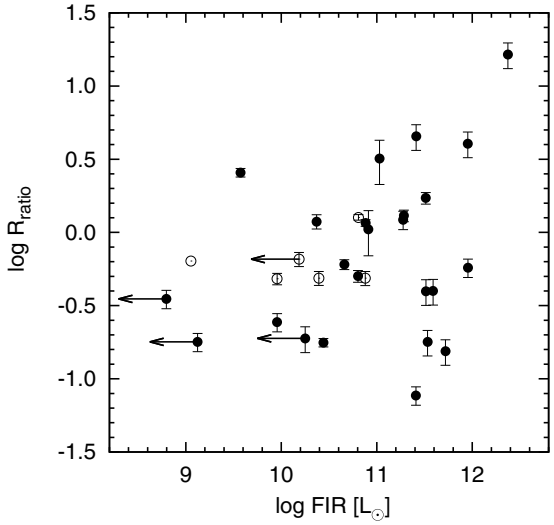

Figure 7. Plot of the FIR luminosity vs. the relative size of the molecular gas extent to the stellar component. The filled circles show Type A and the open circles show Type B.

overestimation of $R_{\rm ratio}$. Another possibility of the large ratio is that $R_{\rm eff}$ is underestimated due to an excess light in the galactic center.

The $R_{\rm ratio}$ of Type A galaxies except for UGC 8058 range between 0.08 and 4.5. The source with the largest $R_{\rm ratio}$ is NGC 34 ($R_{\rm ratio} = 4.5 \pm 0.9$), followed by UGC 5101 ($R_{\rm ratio} = 4.0 \pm 0.8$) and UGC 10675 ($R_{\rm ratio} = 3 \pm 1$). These three sources have relatively high FIR luminosities ($L_{\rm FIR} > 10^{11}\ L_{\odot}$), suggesting that the molecular gas may eventually become the stellar disk. However, the timescale for stellar disk formation is related to the complex interplay among gravitational compression, residual gas inflow, shear motion, stellar feedback, and the gas dynamics in the non-axisymmetric potential, and it may not be easy to determine. In order to confirm the formation of stellar disks, we will have to observe these sources using dense gas and ionized gas tracers at high angular resolution. In addition, there is no relation between the relative size of the molecular gas disk and FIR luminosity for the whole sample (Figure 7). While half of the U/LIRGs in our sample have compact disks that are consistent with previous studies (Downes & Solomon 1998), the rest of U/LIRGs have extended molecular gas disks. Therefore the formation of extended molecular gas disks is not related to the physical activity that increases the FIR luminosity, namely, the starburst/AGN.

We find that the molecular gas disks in 54% (13/24) of the sources are more compact than the K-band effective radius. These gas disks may have formed by past gas inflow that was triggered by dynamical instability during the merging event (Barnes 2002) or dry mergers. Since the molecular gas is already concentrated in the nuclear regions as seen in present day early-type galaxies (e.g., Crocker et al. 2011; Alatalo et al. 2013; Davis et al. 2013), these sources are candidates which could become early-type galaxies in the future. On the other hand, the molecular gas disks in 46% (11/24) of the sources are larger than the K-band effective radius. The frequent occurrence of large gas disks suggest the possibility that merging galaxies can evolve into bulge-dominated late-type galaxies unless there are further mechanisms to transport the molecular gas toward the central region (e.g., nuclear bar; Bournaud & Combes 2002) and decrease the size of the molecular gas disk. The ubiquitous presence of both compact and extended gas disks is consistent with the numerical predictions that mergers of gas-rich galaxies can produce both early- and late-type galaxy population (Springel & Hernquist 2005).

5.4. Implications for Galaxies at $z = 1$ to 3

Understanding the process of disk formation is particularly important at high-redshift when morphological segregation into different Hubble types begins. However, the exact formation mechanism of disk galaxies is not well understood. Two commonly adopted scenarios are major mergers of gas-rich progenitor disks (e.g., Robertson & Bullock 2008), or cosmological inflow of low-angular momentum cold gas that eventually settles onto the galactic disks (e.g., Kereš et al. 2005; Dekel et al. 2009). Recent high-sensitivity submillimeter observations and optical integral field spectroscopy reveal the presence of molecular and ionized gas disks in star-forming galaxies at high redshift (e.g., Förster Schreiber et al. 2006; Tacconi et al. 2013). Tacconi et al. (2013) classify 50%–75% of their sample of $z = 1$–3 galaxies as disk/spiral galaxies based on the CO kinematics and stellar morphology.

An important finding from our CO study of merger remnants is the high occurrence rate of molecular gas disks with various sizes, some of which are approaching the size of the Milky Way disk. While the surrounding environment and the properties of the progenitor disks may be different at low and high redshifts, this suggests the possibility that a good fraction of what are identified as disk galaxies (i.e., favoring the cold accretion model) at high redshifts through rotational kinematics may in fact contain a substantial subset of merger remnants. Deep- and high-resolution imaging of the rest-frame K-band emission is needed in order to understand the true nature of these sources. Finally, we note that the initial collision of our sample sources probably occurred a few billion years ago (∼typical merger timescale), and the observational evidence of high (>30%) gas mass fraction even at $z = 0.3$ (3 Gyr ago) (e.g., Daddi et al. 2010; Combes et al. 2013) is consistent with the theoretical prediction that disks with higher gas mass fraction are more likely to survive the collision (see discussion in Introduction, and in Hopkins et al. 2009).

6. SUMMARY

We have conducted a CO imaging study of optically selected merger remnants in the local universe using millimeter/submillimeter interferometers including ALMA, CARMA, and SMA in order to investigate the properties of molecular gas in merger remnants. We also obtained archival interferometric data from ALMA, IRAM PdBI, and SMA for 10 further galaxies, forming a grand sample of 37 merger remnants. In addition, new NRO 45 m telescope data and earlier single-dish measurements from the IRAM 30 m, SEST 15 m, FCRAO 14 m, and NRAO 12 m telescopes were obtained to analyze the total CO flux.

We investigate interferometric CO maps of 37 merger remnants, including 7 galaxies which were undetected in the CO line, and find that 80% (24/30) of the sample with robust CO detections show kinematical signatures of rotating molecular gas disks. We also find that the emission peaks in a PV diagram are clearly shifted from the galactic centers in 75% (18/24) sources with molecular gas disks, suggesting the presence of a ring and/or a bar. The CO distribution of the remaining six galaxies is not characterized by simple gas disk model. These sources show clumpy CO distributions and complex velocity fields, indicating that the molecular gas is still strongly disturbed and has not settled in the galactic plane. The molecular gas masses range between 10^7 $M_\odot$and 10^{11} $M_\odot$, adopting standard CO luminosity-to-H_2 conversion factors.

The sizes of the molecular gas disks ($R_{\rm CO}$) vary significantly from 1.1 kpc to 9.3 kpc with an average of 3.5 $\pm$ 2.3 kpc. We also estimate the size ratio of the molecular gas disk to the stellar component for 24 merger remnants in order to investigate whether cold molecular gas disks are in extended form, as predicted from recent numerical simulations. The size ratios for 54% (13/24) of the sample are less than unity, hence these sources have compact molecular gas disks as seen in present day early-type galaxies. These disks may have formed by past gas inflow that was triggered by dynamical instability following the merging. On the other hand, 46% (11/24) of the sample have gas disks that are extended relative to the stellar component. We suggest the possibility that these extended gas disks may be rebuilding stellar disks and forming a late-type galaxy.

The CO data products of 17 merger remnants that we observed will be publicly released on the Web site (http://alma-intweb.mtk.nao.ac.jp/ jueda/data.html). The products include data cubes, integrated intensity maps, and velocity fields in FITS format.

We thank L. K. Hunt, S. García-Burillo, E. Juette, B. Rothberg, and C. D. Wilson for kindly providing their published data. We also thank Chihomi Hara for her help on preparing the CARMA observing scripts. We would like to express our gratitude to the EA-ARC, SMA, and CARMA staff members for making the new observations possible.

This paper has made use of the following ALMA data: ADS/JAO.ALMA#2011.0.00099.S and ALMA Science Verification data: ADS/JAO.ALMA#2011.0.00002.SV. ALMA is a partnership of the ESO (representing its member states), NSF (USA), and NINS (Japan), together with the NRC (Canada), NSC, and ASIAA (Taiwan), in cooperation with the Republic of Chile. The Joint ALMA Observatory is operated by the ESO, AUI/NRAO, and NAOJ.

The Submillimeter Array is a joint project between the Smithsonian Astrophysical Observatory and the Academia Sinica Institute of Astronomy and Astrophysics and is funded by the Smithsonian Institution and the Academia Sinica.

Support for CARMA construction was derived from the Gordon and Betty Moore Foundation, the Kenneth T. and Eileen L. Norris Foundation, the James S. McDonnell Foundation, the Associates of the California Institute of Technology, the University of Chicago, the states of California, Illinois, and Maryland, and the National Science Foundation. Ongoing CARMA development and operations are supported by the National Science Foundation under a cooperative agreement and by the CARMA partner universities.

This research has made use of the NASA/IPAC Extragalactic Database (NED), which is operated by the Jet Propulsion Laboratory, California Institute of Technology, under contract with the National Aeronautics and Space Administration.

Finally, J.U. is financially supported by a Research Fellowship from the Japan Society for the Promotion of Science for Young Scientists and the Sasakawa Scientific Research Grant from The Japan Science Society. D.I. is supported by JSPS KAKENHI grant Number 2580016. D.N. acknowledges support from the US NSF via grant AST-144560.

APPENDIX

NOTES ON INDIVIDUAL GALAXIES

This Appendix provides background information on each of the sources revealed in previous observations and numerical simulations. Here we also give a short description of the morphological and kinematical features of the molecular gas seen in the integrated intensity maps, velocity fields, channel maps, and PV diagrams along the kinematic major axis. The rotational velocity of the molecular gas, which we describe in the following subsections, is corrected for inclination using the estimation given in Table 6.

A.1. UGC 6 (VV 806, Mrk 334)

Several loops and shells are identified in this galaxy in optical wavelengths. The *Hubble Space Telescope* (*HST*)/Wide Field and Planetary Camera 2 (WFPC2) *V*-band image clearly shows circumnuclear spiral structures (Martini et al. 2003). The Hα velocity field reveals a rotating disk whose rotational velocity is almost constant ($V_{\rm rot}$ = 210–220 km s^{-1}) over a radial distance range of 4″–12″ (Smirnova & Moiseev 2010). Optical spectroscopy classifies the galaxy as a Seyfert 1.8 (e.g., Dahari & De Robertis 1988; Osterbrock & Martel 1993). The H I spectra show a double-horn profile (Mirabel & Sanders 1988), which is characteristic of a rotating disk.

The CO (1–0) emitting gas is distributed within a radius of 3″ ($\simeq$1.3 kpc) from the galactic center. The detailed distribution and kinematics is not clear due to the limited velocity resolution (ΔV = 100 km s^{-1}), but the velocity field reveals the presence of a rotating disk. The maximum rotational velocity is estimated to be $\sim$280 km s^{-1}. This molecular gas disk is about four times smaller than the ionized gas disk studied by Smirnova & Moiseev (2010).

A.2. NGC 34 (NGC 17, VV 850, Mrk 938)

This galaxy is classified as an LIRG. The galaxy has several ripple-like patterns and two linear tidal tails extending toward the northeast and the southwest seen in the optical. The projected length of the longer tail is over 20 kpc (Schweizer & Seitzer 2007). The *HST*/Advanced Camera for Surveys (ACS) *B*-band image clearly shows a bluish central disk with spirals and its optical light is dominated by a $\sim$400 Myr old post-starburst population (Schweizer & Seitzer 2007). The nature of

the activity in this galaxy based on the optical spectra is controversial. Some authors classify the galaxy as a Seyfert 2 (e.g., Veilleux et al. 1995; Yuan et al. 2010; Brightman & Nandra 2011), while others suggest that the galaxy is classified as a H II galaxy rather than a Seyfert galaxy (e.g., Mulchaey et al. 1996; Gonçalves et al. 1999). Fernández et al. (2010) find two diffuse radio lobes, spanning 390 kpc, which could be a signature of an AGN or a starburst-driven superwind. Fernández et al. (2010) also suggest that an atomic gas disk is forming from the gas of the northern tail. Xu et al. (2014) present ALMA Cycle 0 observations of the CO (6–5) line and find a compact gas disk with a size of 200 pc.

This galaxy has a molecular gas disk extended in comparison with the stellar structure ($R_{80}/R_{\rm eff} = 4.54$), but the absolute size of the molecular gas disk ($R_{\rm CO} \simeq 3$ kpc) is approximately equal to the average size in our sample. The PV diagram shows nearly symmetric isophotes with respect to the systemic velocity and two emission peaks on opposite sides of the nucleus, indicating the presence of a ring or a disk with non-uniform distribution.

A.3. Arp 230 (IC 51)

This galaxy is well known as a shell galaxy and listed as a candidate polar ring galaxy (Whitmore et al. 1990). The *HST*/WFPC2 *V*-band image shows strong dust lanes along the polar ring. Stellar shells are clearly visible in the northeast and southeast. McGaugh & Bothun (1990) estimate the timescale for shell formation based on the optical color of the shells. The color implies an age of 1–2 Gyr for the outermost shell, an age of 0.5–0.7 Gyr for the intermediate shell, and a young age ($\leqslant$0.3 Gyr) for the inner shells. The majority of the 6 cm radio continuum and H I emission is aligned with the optical dust lane (Cox & Sparke 2004; Schiminovich et al. 2013). From the H I velocity field, Schiminovich et al. (2013) find the presence of an outer H I disk and a dense inner H I disk/ring.

The CO (1–0) emitting gas is seen along the optical dust lane and distributed in three main components. One component is associated with the nucleus and the others are located at the tangential points of the polar ring. The velocity field shows a shallow velocity gradient of $\sim$75 km s^{-1} kpc^{-1}, which has been corrected using the estimated inclination of 65°. These signatures suggest the presence of a slow-rotating ring/disk of the molecular gas, which appears to coincide with the inner H I disk/ring (Schiminovich et al. 2013). In addition, we find three 3 mm continuum components, whose peaks roughly correspond to the CO emission peak of the three main components.

A.4. NGC 455 (Arp 164, UGC 815)

There are few studies focusing on this galaxy. Optical imaging reveals two diffuse tails extending toward the northwest and the southeast. The galaxy is undetected in the *IRAS* Sky Survey Atlas, but detected in the *AKARI* All-Sky Survey. We estimate a FIR luminosity of $3.0 \times 10^9\ L_\odot$ using *AKARI* data at 65 μm, 90 μm, and 140 μm (Yamamura et al. 2010) and the formula defined by Takeuchi et al. (2010).

This galaxy is undetected in the CO (1–0) line. The 3σ upper limit on the molecular gas mass is $3.3 \times 10^7\ M_\odot$.

A.5. NGC 828 (UGC 1655)

This galaxy is classified as an LIRG. The NIR image shows several filaments surrounding the main body and spiral features within 10″ from the galactic center (Smith et al. 1996). The small 3.3 μm polycyclic aromatic hydrocarbon (PAH) equivalent width (EW $\leqslant$ 20 nm) suggests that a powerful buried AGN is present in the galaxy (Imanishi 2006). In the Hα emission line, there are three sources with comparable surface brightness (Hattori et al. 2004). One diffuse source is associated with the nucleus and the others are located nearly symmetrically along the major axis of the galaxy. The rotation curve measured from the Hα emission shows flat rotation with a constant velocity ($V_{\rm rot}$ sin i) of 200 km s^{-1} outside $\gtrsim$8″ from the galactic center (Márquez et al. 2002). Multiple CO line spectra show double-horn profiles, suggesting the presence of a rotating disk (Sanders et al. 1991; Casoli et al. 1992; Narayanan et al. 2005). Previous CO (1–0) interferometric observations provide a rotation curve of the molecular gas disk (Wang et al. 1991), but the observed disk size was limited to a 3.5 kpc radius.

Our new CO (2–1) observations confirm the presence of a large molecular gas disk with a radius of 8 kpc. The rotation curve of the molecular gas disk shows flat rotation with a velocity of $\sim$270 km s^{-1} outside a radius of 8″. This rotational velocity is larger than that measured form the Hα emission (Márquez et al. 2002) by 70 km s^{-1}. The PV diagram shows a symmetric distribution and a double peak located at the transition point between rigid rotation and flat rotation, which may signify a spiral and/or a bar structure rather than a ring structure.

A.6. UGC 2238

This galaxy is classified as an LIRG. The Hα emission is distributed across the galaxy in several knots (Hattori et al. 2004). According to optical spectroscopy, Veilleux et al. (1995) classify the galaxy as a Low Ionization Nuclear Emission Region galaxy (LINER), while Yuan et al. (2010) suggest that this is a starburst–AGN composite. However, there is no sign of an AGN or an obscured AGN in the NIR spectra (Imanishi et al. 2010). The radio continuum emission is elongated in the northeast and southwest, corresponding to the optical morphology (Condon et al. 1990).

We find a large molecular gas disk in this galaxy for the first time with a radius of 8.5 kpc. The CO (2–1) emitting gas is elongated in the direction of the morphological major axis of the stellar component. The rotation curve of the molecular gas disk shows flat rotation with a velocity of $\sim$200 km s^{-1} at $\gtrsim$6″ from the galactic center. The PV diagram reveals nearly symmetric isophotes and a double peak located at the transition point between rigid rotation and flat rotation.

A.7. NGC 1210 (AM 0304–255)

This galaxy presents shells in optical images (Malin & Carter 1983). The *K*-band surface brightness is approximately a de Vaucouleurs profile with a the Sérsic index of 4.08 (RJ04). The UV imaging reveals a tidal tail extending toward the north and a diffuse debris structure on the south region (Marino et al. 2009). Furthermore, several UV knots with a luminosity similar to that of the nucleus are seen along the tidal tail. The H I emission observed by Schiminovich et al. (2001) corresponds to the tidal tail visible in the UV images. The PV diagram measured from the [O II] line at 4959 Å shows rigid rotation, suggesting a rotating ionized gas component (Longhetti et al. 1998).

This galaxy is undetected in the CO (1–0) line. The 3σ upper limit on the molecular gas mass is $1.7 \times 10^7\ M_\odot$.

A.8. AM 0318–230

There are few studies focusing on this galaxy. The *K*-band isophotal shape clearly shows a featureless rectangular core, even though the overall shape is dominated by disky isophotes (Chitre & Jog 2002, RJ04).

This galaxy is undetected in the CO (1–0) line. The 3σ upper limit on the molecular gas mass is $2.2 \times 10^8\ M_\odot$.

A.9. NGC 1614 (Arp 186, Mrk 617)

This galaxy is classified as an LIRG. Optical imaging shows a bright center with two spiral arms at scales of few kiloparsecs, a liner tail extending over 20 kpc toward the southwest (Mullan et al. 2011), and a large curved extension to the southeast of the nucleus. The H I map shows a single tail (Hibbard & Yun 1996), which does not follow the optical tail. Several knots and condensations traced by the Hα and the Pα emission are distributed along the eastern spiral arm (Alonso-Herrero et al. 2001; Rodríguez-Zaurín et al. 2011). A star-forming ring with a radius of ~300 pc is observed at the Pα emission (Alonso-Herrero et al. 2001) and radio (e.g., Neff et al. 1990; Olsson et al. 2010). Haan et al. (2011) suggest that the galaxy built up a central stellar cusp due to nuclear starbursts, judging from the significant core light excess in the *H*-band image and relatively large 6.2 μm PAH EW. Soifer et al. (2001) find that 87% of the 12 μm flux come from within a radius of 4″ (1.2 kpc) from the nucleus. This galaxy is classified as a starburst-dominated galaxy with no AGN signature through optical and infrared spectroscopy (e.g., Veilleux et al. 1995; Imanishi et al. 2010). Small HCN/HCO$^+$ line ratios are further evidence for dominance of starburst activity (Costagliola et al. 2011; Imanishi & Nakanishi 2013). High-resolution CO (2–1) observations at 0.″5 resolution reveals a nuclear ring of molecular gas (König et al. 2013) fed by dust lanes.

We use the CO (2–1) data obtained by Wilson et al. (2008). The PV diagram shows rigid rotation and a double peak located at a distance of 300–400 pc from the galactic center, which is consistent with the CO (1–0) data obtained at the Owens Valley Radio Observatory (OVRO; Olsson et al. 2010). This CO (2–1) data is unable to spatially resolve the nuclear molecular ring presented by König et al. (2013).

A.10. Arp 187

This is a well-known radio galaxy. Many radio continuum surveys including Arp 187 have been conducted, but there are few studies focusing on this galaxy using all available wavelengths. Optical imaging shows two diffuse tails running in the north and south directions. Evans et al. (2005) suggest that the star formation rate (SFR) is low because the galaxy has a low $L_{\rm IR}/L_{\rm CO}$, which is similar to the global $L_{\rm IR}/L_{\rm CO}$ of local spiral galaxies, and the dust temperature is lower (30–45 K) than the typical value of radio galaxies. Assuming that the IR luminosity is entirely due to star formation, the SFR derived from the FIR luminosity is a few solar masses per year.

The CO (1–0) emitting gas appears to form a disk overall, but the distribution is disturbed and warped in the nuclear region. We detect two 3 mm continuum components located at both sides of the nucleus, spanning 4 kpc. The direction connecting these two components is different from the kinematical major axis of the molecular gas. These components can be small radio lobes, if an AGN exists. In order to check for the presence of an AGN, we estimate the q value of the radio–FIR correlation (Helou et al. 1985) using the 1.4 GHz radio continuum data (Condon et al. 1998). Arp 187 shows a radio-excess ($q = -0.1$), suggesting an AGN activity. We also investigate the radio spectral index at a few GHz using the 5 GHz and 8.4 GHz radio data from the literature (Wright & Otrupcek 1992). We find a spectral index of $\alpha = -1.0$, which also indicates the presence of an AGN.

A.11. AM 0612–373

There are few studies focusing on this galaxy. Optical imaging shows a long tail extending over 30 kpc toward the south and a dust lane running along the morphological minor axis of the stellar body (Smith & Hintzen 1991). The rotation curve measured from the Ca II triplet absorption line ($\lambda \sim 0.85\,\mu$m) reveals a velocity gradient ($V_{\rm rot} \sin i = \pm 160$ km s^{-1}; Rothberg & Fischer 2010), which cannot be fully explained by either rigid or flat rotation.

Most of the CO (1–0) emitting gas is distributed within a radius of 2.5 kpc from the galactic center. We note that the kinematical major axis of the CO distribution is perpendicular to the apparent morphological major axis of the stellar body. The PV diagram shows rigid rotation and a multi-peak. The maximum rotational velocity is estimated to be ~380 km s^{-1}.

A.12. UGC 4079 (Mrk 84)

There are few studies focusing on this galaxy. The *HST*/WFPC2 *B*-band imaging shows clumpy structures in the main body and a faint tail with several blobs, extending toward the northeast. The H I spectra show a double-horn profile with a FWHM of 234 km s^{-1} (Springob et al. 2005).

The new CO (1–0) spectra obtained using the NRO 45 m telescope show a double-horn profile with a FWHM of 240 km s^{-1}, suggesting the presence of a rotating gas disk. However, the galaxy is undetected in the interferometric maps due to the limited sensitivity. Thus the rotating molecular gas disk is not confirmed.

A.13. NGC 2623 (Arp 243, UGC 4509, VV 79)

This galaxy is classified as an LIRG. The optical image reveals two prominent tails extending over 120″ (~43 kpc; 1″ = 0.36 kpc) toward the northeast and the southwest (Soifer et al. 2001). High-resolution *HST*/ACS images reveal ~100 star clusters in the southern region of the nucleus. Optical colors of the clusters are consistent with ages of ~1–100 Myr (Evans et al. 2008). Soifer et al. (2001) find that 80% of the 12 μm flux comes from within a radius of 2″ (~0.7 kpc) from the galactic center. The rotation curves measured form the Hα and the [N II] emission show flat rotation with a constant velocity ($V_{\rm rot} \sin i$) of ~100 ± 50 km s^{-1} (Smith et al. 1996). While Risaliti et al. (2000) find no X-ray evidence for the presence of an AGN, later work shows the signature of a Compton-thick AGN based on the X-ray data (Maiolino et al. 2003). A high HCN/HCO$^+$ line ratio is further evidence for an AGN (HCN/HCO$^+$(1–0) = 1.5; Imanishi et al. 2009). The H I spectra show both emission and absorption, and two distinct absorption features are observed at velocities below and above the systemic velocity of the galaxy (e.g., Biermann et al. 1978; Mirabel & Sanders 1988). The Very Large Array (VLA) H I map shows two tidal tail, which follow the optical tails (Hibbard & Yun 1996).

We use the CO (2–1) data obtained by Wilson et al. (2008). The CO (2–1) emitting gas is distributed within a radius of 3″

($\simeq$1.1 kpc) from the galactic center. This R_{CO} is the smallest of our sample sources with molecular gas disks. The CO (2–1) maps are similar to the CO (1–0) map obtained at the OVRO by Bryant & Scoville (1999). The PV diagram shows rigid rotation and the maximum rotational velocity is estimated to be V_{rot} sin $i = 180$ km s^{-1}.

A.14. NGC 2782 (Arp 215, UGC 4862)

This galaxy has a long H I tail ($\sim$5′) extending toward the northwest and a short H I tail ($\sim$2′) extending toward the east, which is associated with a stellar tail (Smith 1991). The H I velocity field shows the presence of an inner disk counter-rotating with respect to the gas motions in the outer region (Smith 1991). Smith (1994) conclude using a three-body dynamical model that the galaxy is a merger of two disk galaxies with a mass ratio of $\sim$4:1. The *HST*/WFPC2 images reveals a nuclear stellar bar within a radius of 7.″5, which appears to be fueling gas into the nuclear starburst (Jogee et al. 1999). Mullan et al. (2011) identify 87 star cluster candidates in the eastern tail and 10 candidates in the northwestern tail using the *HST*WFPC2 *V*- and *I*-band images. Previous studies considered its nuclear activity to be dominated by a nuclear starburst (e.g., Kinney et al. 1984; Boer et al. 1992), although recent radio and X-ray observations suggest the presence of a hidden AGN (Braatz et al. 2004; Zhang et al. 2006; Krips et al. 2007).

Hunt et al. (2008) investigate the CO (1–0) and CO (2–1) distribution and kinematics using high spatial and velocity resolution maps obtained at the PdBI. The CO emission is aligned along the stellar nuclear bar with two emission peaks on opposite side of the nucleus, spanning $\sim$6″, and distributed in an elongated structure with two spiral arms within a radius of 8″. We estimate the rotation curve of the molecular gas disk and find flat rotation with a velocity of $\sim$260 km s^{-1} outside a radius of 4″. In addition, there are two more extended spiral features extending toward the north and the south. Additional CO interferometric maps were obtained using the OVRO by Jogee et al. (1999). They find that the bar-like gaseous feature is offset in a leading sense with respect to the stellar bar and shows non-circular motion, which suggests gas inflow into the nucleus.

A.15. UGC 5101

This galaxy is classified as an LIRG or a ULIRG depending on the assumed distance, and is well known as an object with a buried AGN based on multi-wavelength observations. Imanishi et al. (2003) detect an absorbed hard X-ray component with a 6.4 keV Fe Kα line, while Armus et al. (2004) detect the 14.3 μm [Ne v] line. These detections indicate the presence of a buried AGN. A high HCN/HCO$^+$ line ratio (= 2.5) is further evidence for dominance of AGN activity (Imanishi 2006). Optical imaging shows a 38 kpc linear tail extending toward the west and a large ring (Surace et al. 2000). Windhorst et al. (2002) suggest the presence of an inclined dusty disk using the *HST*/WFPC2 *I*-band image. The rotation curves measured from the Hα and [N II] emission show flat rotation with a constant velocity (V_{rot} sin i) of $\sim$200 km s^{-1} (Smith et al. 1996).

We use the CO (2–1) data obtained by Wilson et al. (2008). The PV diagram shows rigid rotation and a double peak located at a distance of 400–500 pc from the galactic center. The PdBI CO (1–0) map (Genzel et al. 1998) is similar to the CO (2–1) map (Wilson et al. 2008), but the CO (1–0) emission is more extended than the CO (2–1). Thus the radius of the molecular gas disk which we estimate in this study is underestimated.

A.16. AM 0956–282 (VV 592)

There are few studies focusing on this galaxy. Optical imaging shows a diffuse core with patchy structures. RJ04 could not determine structural parameters of the *K*-band surface brightness due to its disturbed structure. It is possible that the uncertainty of the position of the nucleus defined in the *K*-band peak is a large. This galaxy is detected in the *AKARI* All-Sky Survey, and the FIR luminosity is estimated to be $7.0 \times 10^8\ L_\odot$ using the three bands (65 μm, 90 μm, and 140 μm; Yamamura et al. 2010).

The CO (1–0) emitting gas is distributed in three main components. The molecular gas masses of these components are $4.8 \times 10^7\ M_\odot$, $4.2 \times 10^6\ M_\odot$, and $1.3 \times 10^6\ M_\odot$. The largest mass component is associated with the main body of the galaxy. The position angle of the kinematic major axis is almost 0°, which is not aligned with the apparent isophotal major axis of the stellar body. The PV diagram reveals a velocity gradient, which is steeper in the northern region than the southern region. The intermediate mass component located in the southeast of the largest component shares the same velocity distribution. A diffuse optical counterpart, possibly a short tidal tail is seen in the same region. Thus this component is likely to have been ejected from the main body due to the interaction. The smallest mass component is located in the west of the main body. This component has a stellar counterpart with a weak 3 mm continuum emission associated with it. This component may be a star cluster or a dwarf galaxy.

A.17. NGC 3256 (AM 1025–433, VV 65)

This galaxy is classified as an LIRG. The galaxy has two prominent tidal tails seen in the optical and the H I emission (English et al. 2003). The projected length of the tails are longer than 40 kpc (Mullan et al. 2011). The *K*-band image (RJ04) shows a single nucleus, but a double nucleus separated by $\sim$5″ ($\sim$0.9 kpc) along the north–south direction has been detected in the radio, NIR, and X-ray (Norris & Forbes 1995; Kotilainen et al. 1996; Lira et al. 2002). The SMA CO (2–1) observations also reveal the presence of the double nucleus (Sakamoto et al. 2006). The northern nucleus has been identified as a intense star-forming region with a powerful outflowing galactic wind (Lípari et al. 2000; Lira et al. 2002). While Neff et al. (2003) suggest that the both nuclei may host low-luminosity AGNs using radio and X-ray observations, Jenkins et al. (2004) find no strong evidence for AGNs based on *XMM-Newton* X-ray observations. The *HST*/WFPC2 images shows spiral structures (Laine et al. 2003). Zepf et al. (1999) find more than 1000 young stellar clusters with ages ranging from a few to several hundred Myrs in the inner region (7 kpc $\times$ 7 kpc) using the *HST*/WFPC2 images.

We use the ALMA SV data. The velocity field and PV diagram reveals the presence of a disturbed disk. The rotation curve of the molecular gas disk shows rigid rotation within a radius of 20″. The strongest 3 mm continuum emission in our sample is detected in this galaxy. The SV data was published by Sakamoto et al. (2014), which, combined with their own higher spatial resolution Cycle 0 data, show several arm-like structures (Sakamoto et al. 2014). The SV data by itself is unable to spatially resolve the double nucleus presented by Sakamoto et al. (2006, 2014).

A.18. NGC 3597 (AM 1112–232)

Optical imaging shows plumes elongated in the west of the main body (Lutz 1991). van Driel et al. (1991) detected two radio components at opposite sides of the galactic center. Optical spectroscopy classifies the galaxy as a H II galaxy (e.g., Veilleux et al. 1995; Kewley et al. 2000). Lutz (1991) find a population of 14 blue stellar clusters and later work by Carlson et al. (1999) also find ∼700 compact objects using the *HST*/WFPC2 images, which suggests that the progenitor galaxies were gas-rich.

The CO (1–0) integrated intensity map shows a bar-like structure. The velocity field shows a smooth velocity gradient and the rotation curve of the molecular gas disk shows flat rotation with a velocity of ∼155 km s^{-1} outside a radius of 1 kpc. The 3 mm continuum is roughly distributed along the bar-like CO structure. The strongest peak of the 3 mm continuum is located at a distance of 3.″7 from the galactic center and corresponds to one of the CO peaks.

A.19. AM 1158–333

There are few studies focusing on this galaxy. Optical imaging shows a diffuse extension toward the south of the main stellar body. The main body is elongated in the northeast and southwest. The brightest peak, which we define as the nucleus, is located at the northeast edge. Arp & Madore (1987) classify the galaxy as an elliptical galaxy with jets. The H I spectra show a double-peaked profile with a FWHM of ∼100 km s^{-1} (Theureau et al. 1998).

We detect two molecular gas components traced by the CO (1–0) line. One component is associated with the nucleus. This cannot be resolved due to the limited spatial resolution. The other is distributed below the main body blue-shifted 80 km s^{-1} from the systemic velocity ($V_{\rm sys} = 3027$ km s^{-1}). The molecular gas mass of the component associated with the nucleus is $1.2 \times 10^7\ M_\odot$, which is 2.8 times smaller than that of the other component.

A.20. NGC 4194 (Arp 160, UGC 7241, VV 261, Mrk 201)

This galaxy is known as the "Medusa Merger." The optical morphology is characterized by a diffuse ("hair-like") tail extending over 10 kpc toward the north of the main body. The H I map shows a single ∼50 kpc tail extending toward the opposite side of the optical tail (Manthey et al. 2008). This galaxy is a candidate of a minor merger between a large elliptical and a small spiral galaxy (Manthey et al. 2008). Weistrop et al. (2004) identify 48 UV-bright knots, two-thirds of which are younger than 20 Myr, and suggest that the UV knots will become globular clusters in several Gyr. The HCN/HCO$^+$(1–0) line ratio is less than unity, suggesting a starburst-dominated galaxy (Costagliola et al. 2011). The ionized gas traced by the 12.8 μm [Ne II] line shows a smooth velocity gradient in the north–south direction through the galactic enter (Beck et al. 2014).

The galaxy is unusual in that the CO (2–1) emission is distributed along the optical tail. As seen in the velocity field, the diffuse gas forms three tails in the northern region of the main body. In addition, the CO (2–1) emitting gas appears to be forming a rotating disk in the main body, although the kinematical parameters for the molecular gas cannot be determined because it is difficult to exclude the gaseous tails from the component associated with the main body. These kinematic features are consistent with the OVRO CO (1–0) map (Aalto & Hüttemeister 2000).

A.21. NGC 4441 (UGC 7572)

Optical imaging shows one tidal tail extending toward the north and two shells to the southwest of the main body. This galaxy is a candidate of a merger remnant between a spiral and an elliptical galaxy (Manthey et al. 2008; Jütte et al. 2010). The large-scale H I distribution and kinematics is studied by Manthey et al. (2008) using the Westerbork Radio Synthesis Telescope. The total mass of the atomic gas is $1.46 \times 10^9\ M_\odot$. The H I distribution shows two prominent tidal tails extending more than 40 kpc toward the north and south. The northern tail follows the optical tail closely. The H I velocity field shows simple rotation in the inner region, indicating that the gas has settle down. Its velocity gradient continues into the tidal tails.

Jütte et al. (2010) investigate the CO (1–0) distribution and kinematics using high spatial and velocity resolution maps obtained at the PdBI. Most of the CO emission comes from a central rotating disk with a radius of about 2 kpc. The kinematic major axis of the molecular gas disk is nearly perpendicular to the rotation of large-scale H I structure (Manthey et al. 2008), indicating a kinematically decoupled core. The integrated intensity map we obtained is slightly different from Jütte et al. (2010) due to different clipping levels. In our map, there are CO extensions on the outer side of the molecular gas disk, which appear to be kinematically decoupled from the disk.

A.22. UGC 8058 (Mrk 231)

This galaxy is the only object in our sample to be classified as a ULIRG, and well known as an object which harbors both intense starburst and powerful AGN activities. The fractional contribution of the AGN and the starburst to the bolometric IR luminosity is uncertain. Farrah et al. (2003) suggest that the AGN contributes ∼30% to the IR luminosity, and Veilleux et al. (2009) estimate that the AGN contribution is ∼70%. This galaxy is also characterized by jets and kiloparsec-scale outflows, which are likely the result of the negative feedback from the AGN. The jets and outflows have been detected at radio wavelengths (e.g., Carilli et al. 1998; Lonsdale et al. 2003), and recently detected at millimeter wavelengths (e.g., Feruglio et al. 2010; Aalto et al. 2012). The outflow rate of molecular gas is estimated to be $\sim 700\ M_\odot$ yr^{-1}, which exceeds the ongoing SFR in the host galaxy (Feruglio et al. 2010). Optical imaging shows two tidal tails extending toward the north and south, whose combined projected length is over 70 kpc (Koda & Subaru Cosmos Team 2009). Multi-wavelength observations (at NIR, millimeter, and radio) suggest the presence of a nearly face-on disk (Carilli et al. 1998; Downes & Solomon 1998; Taylor et al. 1999).

We use the CO (3–2) data obtained by Wilson et al. (2008). The CO (3–2) map reveals the presence of a molecular gas disk as previously presented by Downes & Solomon (1998). The maximum extent of the gas disk estimated using the CO (3–2) map is similar to that seen in the PdBI CO (1–0) map (Downes & Solomon 1998). The PV diagram shows a main component which appears to be a gas disk and a high-velocity component located along the line of sight in the direction of the galactic center. This high-velocity component may be part of molecular outflows.

A.23. AM 1255–430

There are few studies focusing on this galaxy. The optical morphology is *X*-shaped with tails and plumes, the longest of which extends over 20 kpc toward the southeast (Smith & Hintzen 1991).

The distribution of the CO (1–0) emitting gas is significantly disturbed. The kinematical parameters for the molecular gas cannot be determined. The channel map (V = 8560–8840 km s^{-1}) shows an arc-like distribution in the northeast region. The molecular gas moves along the arc and merges into a gas component associated with the nucleus.

A.24. AM 1300–233

This galaxy is classified as an LIRG. The *HST*/ACS *B*-band image show a disrupted nuclear region, a small tail extending toward the northeast, and a bright region located at ∼4 kpc southwest of the galactic center. Although this region is identified as a secondary nucleus (Miralles-Caballero et al. 2011), it is likely to be a massive star-forming region (Monreal-Ibero et al. 2010; Rodríguez-Zaurín et al. 2011). Monreal-Ibero et al. (2010) suggest that the mechanism of ionization in the nuclear region is shocks (100–150 km s^{-1}), using the [O I] λ6300/Hα ratio, which is a good tracer of shock-induced ionization. Optical spectroscopy classify the galaxy as an LINER Corbett et al. (2003). There is no sign of either an AGN or an obscured AGN in the NIR spectra (Imanishi et al. 2010).

The CO (1–0) emitting gas appears to form a disk overall, but the distribution is disturbed and warped in the nuclear region. The kinematic major axis of the molecular gas is inconsistent with the morphological major axis of the stellar body. The 3 mm continuum emission is elongated along the kinematic minor axis of the molecular gas.

A.25. NGC 5018

The galaxy has several shells seen in the NUV (Rampazzo et al. 2007) and the optical (Malin & Carter 1983), and it presents a prominent linear dust lane (Fort et al. 1986). Goudfrooij et al. (1994) find extended Hα+[N II] emission. The projected size of the Hα+[N II] emitting region is larger than 40″ (≃7.3 kpc). The rotation curves measured from the Ca II triplet absorption line (λ ∼ 0.85 μm) and the CO stellar absorption line (λ = 2.29 μm) show flat rotation (Rothberg & Fischer 2010), suggesting the presence of a rotating disk. The H I emission is not associated with the nuclear region; however, it is distributed along a filamentary structure connecting between NGC 5018 and its two neighbors, NGC 5022 and MCG 03-34-013 (Kim et al. 1988). This H I filament is a sign of interaction between these galaxies.

This galaxy is undetected in the CO (1–0) line. The 3σ upper limit on the molecular gas mass is 2.3 × 10^7 $M_\odot$. Lees et al. (1991) and Huchtmeier & Tammann (1992) also report a non-detection in their single-dish CO measurements.

A.26. Arp 193 (UGC 8387, VV 821, IC 883)

This galaxy is classified as an LIRG. The *HST*/ACS *B*-band image shows two straight tails emerging almost at 90° angles, and dust lanes across the nuclear region. There are two emission peaks in the nuclear region, spanning ∼340 pc, traced by the IR (Scoville et al. 2000) and the radio (Condon et al. 1991), but the *K*-band image (RJ04) shows a single peak. The rotation curves measured form the Hα and the [N II] emission show flat rotation with a constant velocity ($V_{\rm rot}$ sin i) of 150 km s^{-1} (Smith et al. 1996). The soft X-ray emission is elongated along the morphological minor axis of the stellar body, which is likely associated with outflow driven by a nuclear starburst or AGN (Iwasawa et al. 2011). Optical spectroscopy classify the galaxy as a LINER (Veilleux et al. 1995), while Yuan et al. (2010) suggest that this is a starburst–AGN composite. However, the small HCN/HCO$^+$(1–0) line ratio of 0.9 and the strong 3.3 μm are evidence for starburst activity with no significant AGN contribution (Imanishi et al. 2009).

Three CO interferometric maps were published (Downes & Solomon 1998; Bryant & Scoville 1999; Wilson et al. 2008). We use the CO (3–2) data obtained by Wilson et al. (2008). The PV diagram shows an asymmetric distribution and the presence of a rotating disk. Other CO (1–0) and CO (2–1) interferometric data also shows a nuclear ring or disk of molecular gas (Downes & Solomon 1998; Bryant & Scoville 1999). The CO (3–2) emission is detected outside the extent of the CO (1–0) and CO (2–1) emission, due to the high sensitivity in CO (3–2) measurements.

A.27. AM 1419–263

There are few studies focusing on this galaxy. Optical imaging shows a ∼20 kpc plume elongated in the southwest and northeast and a 4 kpc tail extending toward the south (Smith & Hintzen 1991). Even though the optical structure is strongly distorted, the *K*-band surface brightness is almost perfectly fit by the de Vaucouleurs profile (RJ04). The rotation curve measured from the Ca II triplet absorption line (λ ∼ 0.85 μm) shows a shallow velocity gradient (Rothberg & Fischer 2010), which cannot be fully explained by rigid rotation or flat rotation.

This galaxy is tentatively detected in the CO (1–0) line, but there is no robust emission (>1.5σ) continuing in velocity. The detailed distribution and kinematics of the molecular gas is not clear due to the limited sensitivity. The 3 mm continuum emission is clearly detected at the ∼20σ level in the nucleus.

A.28. UGC 9829 (VV 847)

There are few studies focusing on this galaxy. Optical imaging shows two long tidal tails running north–south. The projected length of the northern tail is longer than 30 kpc. The *K*-band image shows a bar structure across the nucleus (RJ04).

This galaxy is an unusual case in that most of the CO (2–1) emission comes from the root of the northern tail, with only weak emission seen in the nucleus. The molecular gas shows a kinematic signature of gas streaming along the tail, but it does not appear to inflow into the nuclear region because the velocity of the molecular gas in the nucleus is about 250 km s^{-1} smaller than that in the tail leading to the nucleus.

A.29. NGC 6052 (Arp 209, UGC 10182, VV 86, Mrk 297)

The optical morphology is dominated by a large number of clumpy features, which appear to be young massive clusters according to their color and brightness (Holtzman et al. 1996). The H I map shows a tidal tail extending toward the south (Garland et al. 2007). Alloin & Duflot (1979) interpret the galaxy as a merger of two late-type galaxies, which might have produced the burst of star formation in clumps. Taniguchi & Noguchi (1991) suggest from numerical *N*-body simulations of the collision of two disk galaxies that the evolutionary phase of this galaxy corresponds to about 150 Myr after the first impact. The peak of the radio continuum emission is shifted from the emission peak in optical images, suggesting the presence of off-nuclear starbursts (e.g., Condon et al. 1990; Deeg et al. 1993). The OVRO CO (1–0) emission is barely resolved and the size of the CO (1–0) source is 7.″5 × 4.″8 (Garland et al. 2007).

The CO (2–1) emitting gas comes from the northern part of the galaxy and is not associated with the nucleus nor bright knots

in the optical. The velocity field of the molecular gas as well as the ionized gas (García-Lorenzo et al. 2008) are significantly disturbed and shows complex structures. The majority of the molecular gas appears not to rotate in circular motion around the nucleus. It is likely that the galaxy has not undergone violent relaxation, according to the kinematics of the molecular gas and the apparent morphology.

A.30. UGC 10675 (VV 805, Mrk 700)

Optical imaging shows a plume extending toward the southwest of the main body. Optical spectroscopy classifies the galaxy as a Seyfert 1 (Denisiuk et al. 1976; Gallego et al. 1996). However, Gonçalves et al. (1999) suggest that the galaxy is an LINER because the line strengths are weaker than those in classical AGNs. Furthermore, there is no evidence of an AGN from the radio–FIR correlation (Ji et al. 2000).

The CO (2–1) emitting gas appears to form a disk overall, but it is extremely disturbed. The PV diagram reveals three peaks, two of which overlap along the line of sight. There are only three resolution elements along the radial direction due to the limited sensitivity and the low angular resolution. Thus it is possible that derived radial properties have large uncertainties.

A.31. AM 2038–382

Optical imaging shows a plume extending toward the east and a prominent southwest loop. Optical spectroscopy reveals the dominance of A–F-type stars while lacking strong H II region type emission lines, suggesting that the burst of star formation ended less than a few $\times 10^8$ yr ago (Sekiguchi & Wolstencroft 1993). The H I spectrum is roughly a double-horn profile (Richter et al. 1994). The rotation curve measured from the CO stellar absorption line at 2.29 μm, however, shows no sign of a rotating disk (Rothberg & Fischer 2010).

The CO (2–1) integrated intensity map is shaped like a peanut. A peanut-shaped gas distribution is often seen in barred galaxies because gas piles up at the bar ends. The size of the northern concentration is larger than the southern one. The PV diagram shows a velocity gradient of $\sim$260 km s^{-1} kpc^{-1} and two emission peaks, which are offset by 2″ ($\sim$0.8 kpc) from the galactic center. These signatures imply the presence of a ring or a bar, but a bar structure is not identified in optical images.

A.32. AM 2055–425

This galaxy is classified as an LIRG or a ULIRG depending on the assumed distance. The *HST*/ACS *B*-band image shows two tidal tails and knotty structures in the main body. The velocity field of the Hα emission shows rotational motion with a velocity width of 150 km s^{-1} without inclination correction (Mihos & Bothun 1998). Optical spectroscopy classifies the galaxy as a starburst–AGN composite (Yuan et al. 2010; Brightman & Nandra 2011). The IR spectroscopy reveals the presence of a buried AGN (Risaliti et al. 2006; Imanishi et al. 2010) and the X-ray emission is clearly dominated by a hidden AGN (Franceschini et al. 2003).

Most of the CO (1–0) emission comes from the southeast region of the main body, but the emission peaks seen in all channel maps are located at the nucleus. The PV diagram also shows gas concentration in the nucleus. In addition, an extension of the molecular gas is distributed in the southwest region of the main body, which does not correspond to the stellar arm structure. The velocity field in the molecular gas disk shows a less distinct velocity gradient due to the low inclination of the molecular gas disk ($i = 10°$) and non-circular motion. The 3 mm continuum emission is associated with the nucleus and the peak corresponds to the CO peak seen in the integrated intensity map.

A.33. NGC 7135 (AM 2146–350, IC 5136)

This galaxy has shell structures seen in the optical (Malin & Carter 1983) as well as in the UV (Rampazzo et al. 2007). The distribution of warm ionized gas shows an asymmetric structure relative to the stellar body, elongated in the southwest direction (Rampazzo et al. 2003), which corresponds to the FUV distribution. The velocity field of warm ionized gas indicates rotational motion with a maximum rotation velocity ($V_{\rm rot}$ sin i) of 78 km s^{-1} (Rampazzo et al. 2003). Rampazzo et al. (2007) suggest, using the relation between the optical line-strength indices and UV colors, that the galaxy experienced recent nuclear star formation likely triggered by the interaction/accretion that formed the shells. The VLA H I emission is mostly detected outside the main body (Schiminovich et al. 2001).

The CO (1–0) emitting gas is distributed in the southern region of the main body and not associated with the nucleus. The detailed structure and kinematics of the molecular gas are not clear due to the weak CO emission. The 3 mm continuum emission is robustly detected and the peak of the continuum emission corresponds to the nucleus.

A.34. NGC 7252 (Arp 226, AM 2217-245)

This galaxy is a well-known merger, called the "Atoms for Peace." The galaxy has remarkable loops and two long tidal tails seen in the optical. High-resolution optical imaging carried out using the *HST*/WFPC reveals spiral arms within a radius of 3.″5 from the galactic center and weak spiral features out to about 9″ (Whitmore et al. 1993). Miller et al. (1997) detect 499 cluster candidates, whose mean age is estimated to be 0.6 $\pm$ 0.2 Gyr by Whitmore et al. (1997). The H I emission is associated with the optical tidal tails, whose projected length are 520″ and 270″ (Hibbard et al. 1994), corresponding to 160 kpc and 82 kpc, respectively. Schweizer et al. (2013) suggest that the atomic gas is falling back to the nucleus. Previous CO (1–0) interferometric observations show a rotating molecular gas disk (Wang et al. 1992), but the observed disk size was limited to a $\sim$1.2 kpc radius.

Numerical simulations focusing on this galaxy have been conducted (e.g., Borne & Richstone 1991; Hibbard & Mihos 1995; Chien & Barnes 2010). They conclude that the galaxy is a merger between two disk galaxies and resulting in an elliptical galaxy. The merger age is estimated to be about 0.5–1 Gyr from numerical simulations (Hibbard & Mihos 1995; Chien & Barnes 2010) as well as observations (Schweizer 1982). This is in good agreement with the mean age of the star clusters (Whitmore et al. 1997). Mihos et al. (1993) suggest that the SFR has fallen to one-third of the value that it would have been at its peak according their simulation.

Our new CO (1–0) observations confirm the presence of a molecular gas disk two times larger ($R_{\rm CO} = 2.6$ kpc) than the previous results (Wang et al. 1992). The velocity field shows a smooth velocity gradient, and the rotation curve of the molecular gas disk shows flat rotation with a velocity of $\sim$260 km s^{-1} outside a radius of 1 kpc. The PV diagram shows a double peak located at the transition point between rigid rotation and flat rotation. The 3 mm continuum emission is detected around the nucleus at the 4σ level.

A.35. AM 2246–490

This galaxy is classified as an LIRG or a ULIRG depending on the assumed distance. The *HST*/ACS *B*-band image shows a single nucleus with long prominent tails. Haan et al. (2011) suggest that the galaxy built up a central stellar cusp due to nuclear starbursts, judging from the significant core light excess in the *H*-band image and relatively large 6.2 μm PAH EW. While optical spectroscopy classifies the galaxy as a Seyfert 2 (Yuan et al. 2010), there is no signature of an AGN according to a selection by hard X-ray color and the 6.4 keV iron line (Iwasawa et al. 2011).

The velocity field shows the presence of a warped gas disk. The PV diagram reveals rigid rotation and a double peak located off-center, suggesting the possibility of a ring structure, but a non-uniform distribution of molecular gas may also explain the observed diagram. The 3 mm continuum emission is associated with the nucleus and the peak corresponds to the CO peak seen in the integrated intensity map.

A.36. NGC 7585 (Arp 223)

This galaxy has shells seen in the optical (Malin & Carter 1983). Multicolor optical imaging reveals that the shells are bluer than the main body, and that the timescale from the interaction, by which the shells were formed, is typically $\sim$1 Gyr (McGaugh & Bothun 1990). The upper limit of the atomic gas mass is $7.5 \times 10^9\ M_\odot$ (Balick et al. 1976).

The galaxy is undetected in the CO (1–0) line. The 3σ upper limit on the molecular gas mass is $3.1 \times 10^7\ M_\odot$. Georgakakis et al. (2001) also report non-detection in their CO measurements obtained at the OSO 20 m telescope.

A.37. NGC 7727 (Arp 222, VV 67)

The *HST*/WFPC2 *B*-band image reveals spiral structures (Peeples & Martini 2006), while the *K*-band surface brightness profile roughly follows the de Vaucouleurs law (Chitre & Jog 2002, RJ04). The Hα emission is associated with the nuclear region (Knapen 2005), where the mean stellar color is slightly bluer than the outer envelopes (Schombert et al. 1990). The rotation curve measured from the Mg_b absorption line ($\lambda \sim 0.52\ \mu$m) reveals a velocity gradient ($V_{\rm rot} \sin i = \pm 150$ km s^{-1}; Simien & Prugniel 1997). This galaxy is detected in the *AKARI* All-Sky Survey, and the FIR luminosity is estimated to be $4.5 \times 10^8\ L_\odot$ using three bands (65 μm, 90 μm, and 140 μm; Yamamura et al. 2010).

The PV digram shows rigid rotation, suggesting the presence of a rotating gas disk. The maximum rotational velocity is estimated to be $\sim$150 km s^{-1}. A close inspection of the channel maps reveals two different components. The low-velocity component ($V = 1665$–1735 km s^{-1}) is associated with the nucleus and the high-velocity component ($V = 1740$–1990 km s^{-1}) is distributed along the optical dust lane. The molecular gas mass in the high-velocity component is nearly eight times larger than that in the low-velocity component. The 3 mm continuum emission is associated with the nucleus and the peak corresponds to the CO peak seen in the integrated intensity map.

REFERENCES

Aalto, S., Garcia-Burillo, S., Muller, S., et al. 2012, A&A, 537, A44
Aalto, S., & Hüttemeister, S. 2000, A&A, 362, 42
Alatalo, K., Davis, T. A., Bureau, M., et al. 2013, MNRAS, 432, 1796
Albrecht, M., Chini, R., Krügel, E., Müller, S. A. H., & Lemke, R. 2004, A&A, 414, 141
Albrecht, M., Krügel, E., & Chini, R. 2007, A&A, 462, 575
Alloin, D., & Duflot, R. 1979, A&A, 78, L5
Alonso-Herrero, A., Engelbracht, C. W., Rieke, M. J., Rieke, G. H., & Quillen, A. C. 2001, ApJ, 546, 952
Andreani, P., Casoli, F., & Gerin, M. 1995, A&A, 300, 43
Armus, L., Charmandaris, V., Spoon, H. W. W., et al. 2004, ApJS, 154, 178
Arp, H. C., & Madore, B. 1987, Cambridge (Cambridge, New York: Univ. Press)
Balick, B., Faber, S. M., & Gallagher, J. S. 1976, ApJ, 209, 710
Barnes, J. E. 2002, MNRAS, 333, 481
Barnes, J. E., & Hernquist, L. 1992, ARA&A, 30, 705
Beck, S. C., Lacy, J., Turner, J., Greathouse, T., & Neff, S. 2014, ApJ, 787, 85
Beichman, C. A., Neugebauer, G., Habing, H. J., Clegg, P. E., & Chester, T. J. 1988, Infrared Astronomical Satellite (IRAS) Catalogs and Atlases. Volume 1: Explanatory Supplement (Washington, DC: NASA), 1
Bertram, T., Eckart, A., Krips, M., Staguhn, J. G., & Hackenberg, W. 2006, A&A, 448, 29
Biermann, P., Clarke, J. N., & Fricke, K. J. 1978, A&A, 70, L41
Boer, B., Schulz, H., & Keel, W. C. 1992, A&A, 260, 67
Borne, K. D., & Richstone, D. O. 1991, ApJ, 369, 111
Bournaud, F., & Combes, F. 2002, A&A, 392, 83
Braatz, J. A., Henkel, C., Greenhill, L. J., Moran, J. M., & Wilson, A. S. 2004, ApJL, 617, L29
Bridge, C. R., Carlberg, R. G., & Sullivan, M. 2010, ApJ, 709, 1067
Brightman, M., & Nandra, K. 2011, MNRAS, 414, 3084
Bryant, P. M., & Scoville, N. Z. 1999, AJ, 117, 2632
Cappellari, M., Emsellem, E., Krajnović, D., et al. 2011, MNRAS, 413, 813
Carilli, C. L., & Walter, F. 2013, ARA&A, 51, 105
Carilli, C. L., Wrobel, J. M., & Ulvestad, J. S. 1998, AJ, 115, 928
Carlson, M. N., Holtzman, J. A., Grillmair, C. J., et al. 1999, AJ, 117, 1700
Casey, C. M., Narayanan, D., & Cooray, A. 2014, arXiv:1402.1456
Casoli, F., Dupraz, C., & Combes, F. 1992, A&A, 264, 49
Chien, L.-H., & Barnes, J. E. 2010, MNRAS, 407, 43
Chitre, A., & Jog, C. J. 2002, A&A, 388, 407
Combes, F., García-Burillo, S., Braine, J., et al. 2013, A&A, 550, A41
Condon, J. J., Anderson, M. L., & Helou, G. 1991, ApJ, 376, 95
Condon, J. J., Cotton, W. D., Greisen, E. W., et al. 1998, AJ, 115, 1693
Condon, J. J., Helou, G., Sanders, D. B., & Soifer, B. T. 1990, ApJS, 73, 359
Corbett, E. A., Kewley, L., Appleton, P. N., et al. 2003, ApJ, 583, 670
Costagliola, F., Aalto, S., Rodriguez, M. I., et al. 2011, A&A, 528, A30
Cox, A. L., & Sparke, L. S. 2004, AJ, 128, 2013
Crocker, A. F., Bureau, M., Young, L. M., & Combes, F. 2011, MNRAS, 410, 1197
Daddi, E., Bournaud, F., Walter, F., et al. 2010, ApJ, 713, 686
Dahari, O., & De Robertis, M. M. 1988, ApJS, 67, 249
Davis, T. A., Alatalo, K., Bureau, M., et al. 2013, MNRAS, 429, 534
Dasyra, K. M., Tacconi, L. J., Davies, R. I., et al. 2006, ApJ, 651, 835
Deeg, H.-J., Brinks, E., Duric, N., Klein, U., & Skillman, E. 1993, ApJ, 410, 626
Dekel, A., Birnboim, Y., Engel, G., et al. 2009, Natur, 457, 451
Denisiuk, E. K., Lipovetskii, V. A., & Afanasev, V. L. 1976, Afz, 12, 665
Downes, D., & Solomon, P. M. 1998, ApJ, 507, 615
English, J., Norris, R. P., Freeman, K. C., & Booth, R. S. 2003, AJ, 125, 1134
Evans, A. S., Mazzarella, J. M., Surace, J. A., et al. 2005, ApJS, 159, 197
Evans, A. S., Vavilkin, T., Pizagno, J., et al. 2008, ApJL, 675, L69
Farrah, D., Afonso, J., Efstathiou, A., et al. 2003, MNRAS, 343, 585
Fernández, X., van Gorkom, J. H., Schweizer, F., & Barnes, J. E. 2010, AJ, 140, 1965
Feruglio, C., Maiolino, R., Piconcelli, E., et al. 2010, A&A, 518, L155
Förster Schreiber, N. M., Genzel, R., Lehnert, M. D., et al. 2006, ApJ, 645, 1062
Fort, B. P., Prieur, J.-L., Carter, D., Meatheringham, S. J., & Vigroux, L. 1986, ApJ, 306, 110
Franceschini, A., Braito, V., Persic, M., et al. 2003, MNRAS, 343, 1181
Gallego, J., Zamorano, J., Rego, M., Alonso, O., & Vitores, A. G. 1996, A&AS, 120, 323
Galletta, G., Sage, L. J., & Sparke, L. S. 1997, MNRAS, 284, 773
García-Lorenzo, B., Cairós, L. M., Caon, N., Monreal-Ibero, A., & Kehrig, C. 2008, ApJ, 677, 201
Garland, C. A., Pisano, D. J., Williams, J. P., et al. 2007, ApJ, 671, 310
Genzel, R., Lutz, D., Sturm, E., et al. 1998, ApJ, 498, 579
Genzel, R., Tacconi, L. J., Rigopoulou, D., Lutz, D., & Tecza, M. 2001, ApJ, 563, 527
Georgakakis, A., Hopkins, A. M., Caulton, A., et al. 2001, MNRAS, 326, 1431
Gonçalves, A. C., Véron-Cetty, M.-P., & Véron, P. 1999, A&AS, 135, 437
Goudfrooij, P., Hansen, L., Jorgensen, H. E., & Norgaard-Nielsen, H. U. 1994, A&AS, 105, 341
Haan, S., Surace, J. A., Armus, L., et al. 2011, AJ, 141, 100
Hattori, T., Yoshida, M., Ohtani, H., et al. 2004, AJ, 127, 736

Helfer, T. T., Thornley, M. D., Regan, M. W., et al. 2003, ApJS, 145, 259
Helou, G., Soifer, B. T., & Rowan-Robinson, M. 1985, ApJL, 298, L7
Hibbard, J. E., Guhathakurta, P., van Gorkom, J. H., & Schweizer, F. 1994, AJ, 107, 67
Hibbard, J. E., & Mihos, J. C. 1995, AJ, 110, 140
Hibbard, J. E., & Yun, M. S. 1996, in Cold Gas at High Redshift, ed. M. N. Bremer & N. Malcolm (Astrophysics and Space Science Library, Vol. 206; Dordrecht: Kluwer), 47
Holtzman, J. A., Watson, A. M., Mould, J. R., et al. 1996, AJ, 112, 416
Hopkins, P. F., Cox, T. J., Younger, J. D., & Hernquist, L. 2009, ApJ, 691, 1168
Horellou, C., & Booth, R. 1997, A&AS, 126, 3
Huchtmeier, W. K., & Tammann, G. A. 1992, A&A, 257, 455
Hunt, L. K., Combes, F., García-Burillo, S., et al. 2008, A&A, 482, 133
Imanishi, M. 2006, AJ, 131, 2406
Imanishi, M., Nakagawa, T., Shirahata, M., Ohyama, Y., & Onaka, T. 2010, ApJ, 721, 1233
Imanishi, M., & Nakanishi, K. 2013, AJ, 146, 47
Imanishi, M., Nakanishi, K., Tamura, Y., & Peng, C.-H. 2009, AJ, 137, 3581
Imanishi, M., Terashima, Y., Anabuki, N., & Nakagawa, T. 2003, ApJL, 596, L167
Iono, D., Wilson, C. D., Yun, M. S., et al. 2009, ApJ, 695, 1537
Iwasawa, K., Sanders, D. B., Teng, S. H., et al. 2011, A&A, 529, A106
James, P., Bate, C., Wells, M., Wright, G., & Doyon, R. 1999, MNRAS, 309, 585
Jenkins, L. P., Roberts, T. P., Ward, M. J., & Zezas, A. 2004, MNRAS, 352, 1335
Ji, L., Chen, Y., Huang, J. H., Gu, Q. S., & Lei, S. J. 2000, A&A, 355, 922
Jogee, S., Kenney, J. D. P., & Smith, B. J. 1999, ApJ, 526, 665
Jütte, E., Aalto, S., & Hüttemeister, S. 2010, A&A, 509, A19
Kereš, D., Katz, N., Weinberg, D. H., & Davé, R. 2005, MNRAS, 363, 2
Kewley, L. J., Heisler, C. A., Dopita, M. A., et al. 2000, ApJ, 530, 704
Kim, D.-W., Jura, M., Guhathakurta, P., Knapp, G. R., & van Gorkom, J. H. 1988, ApJ, 330, 684
Kinney, A. L., Bregman, J. N., Huggins, P. J., Glassgold, A. E., & Cohen, R. D. 1984, PASP, 96, 398
Knapen, J. H. 2005, A&A, 429, 141
Koda, J., & Subaru Cosmos Team 2009, in ASP Conf. Ser. 408, The Starburst-AGN Connection, ed. W. Wang, Z. Yang, Z. Luo, & Z. Chen (San Francisco, CA: ASP), 22
König, S., Aalto, S., Muller, S., Beswick, R. J., & Gallagher, J. S. 2013, A&A, 553, A72
Kotilainen, J. K., Moorwood, A. F. M., Ward, M. J., & Forbes, D. A. 1996, A&A, 305, 107
Krips, M., Eckart, A., Krichbaum, T. P., et al. 2007, A&A, 464, 553
Laine, S., van der Marel, R. P., Rossa, J., et al. 2003, AJ, 126, 2717
Lake, G., & Dressler, A. 1986, ApJ, 310, 605
Lees, J. F., Knapp, G. R., Rupen, M. P., & Phillips, T. G. 1991, ApJ, 379, 177
Lin, L., Koo, D. C., Willmer, C. N. A., et al. 2004, ApJL, 617, L9
Lípari, S., Díaz, R., Taniguchi, Y., et al. 2000, AJ, 120, 645
Lira, P., Ward, M., Zezas, A., Alonso-Herrero, A., & Ueno, S. 2002, MNRAS, 330, 259
Longhetti, M., Rampazzo, R., Bressan, A., & Chiosi, C. 1998, A&AS, 130, 267
Lonsdale, C. J., Lonsdale, C. J., Smith, H. E., & Diamond, P. J. 2003, ApJ, 592, 804
Lutz, D. 1991, A&A, 245, 31
Maiolino, R., Comastri, A., Gilli, R., et al. 2003, MNRAS, 344, L59
Maiolino, R., Ruiz, M., Rieke, G. H., & Papadopoulos, P. 1997, ApJ, 485, 552
Malin, D. F., & Carter, D. 1983, ApJ, 274, 534
Manthey, E., Aalto, S., Hüttemeister, S., & Oosterloo, T. A. 2008, A&A, 484, 693
Mao, R.-Q., Schulz, A., Henkel, C., et al. 2010, ApJ, 724, 1336
Marino, A., Iodice, E., Tantalo, R., et al. 2009, A&A, 508, 1235
Márquez, I., Masegosa, J., Moles, M., et al. 2002, A&A, 393, 389
Martini, P., Regan, M. W., Mulchaey, J. S., & Pogge, R. W. 2003, ApJS, 146, 353
McGaugh, S. S., & Bothun, G. D. 1990, AJ, 100, 1073
Mihos, J. C., & Bothun, G. D. 1998, ApJ, 500, 619
Mihos, J. C., Bothun, G. D., & Richstone, D. O. 1993, ApJ, 418, 82
Miller, B. W., Whitmore, B. C., Schweizer, F., & Fall, S. M. 1997, AJ, 114, 2381
Mirabel, I. F., Booth, R. S., Johansson, L. E. B., Garay, G., & Sanders, D. B. 1990, A&A, 236, 327
Mirabel, I. F., & Sanders, D. B. 1988, ApJ, 335, 104
Miralles-Caballero, D., Colina, L., Arribas, S., & Duc, P.-A. 2011, AJ, 142, 79
Monreal-Ibero, A., Arribas, S., Colina, L., et al. 2010, A&A, 517, A28
Moshir, M., Kopan, G., Conrow, T., et al. 2008, yCat, 2275, 0
Moshir, M., Kopman, G., & Conrow, T. A. O. 1992, in Explanatory Supplement to the IRAS Faint Source Survey, Version 2, ed. M. Moshir, G. Kopman, & T. A. O. Conrow (Pasadena, CA: JPL), JPL D-10015 8/92
Mulchaey, J. S., Wilson, A. S., & Tsvetanov, Z. 1996, ApJS, 102, 309
Mullan, B., Konstantopoulos, I. S., Kepley, A. A., et al. 2011, ApJ, 731, 93
Naab, T., & Burkert, A. 2003, ApJ, 597, 893
Nakajima, T., Sakai, T., Asayama, S., et al. 2008, PASJ, 60, 435
Nakanishi, H., & Sofue, Y. 2006, PASJ, 58, 847
Narayanan, D., Groppi, C. E., Kulesa, C. A., & Walker, C. K. 2005, ApJ, 630, 269
Narayanan, D., Krumholz, M. R., Ostriker, E. C., & Hernquist, L. 2012, MNRAS, 421, 3127
Neff, S. G., Hutchings, J. B., Standord, S. A., & Unger, S. W. 1990, AJ, 99, 1088
Neff, S. G., Ulvestad, J. S., & Campion, S. D. 2003, ApJ, 599, 1043
Norris, R. P., & Forbes, D. A. 1995, ApJ, 446, 594
Olsson, E., Aalto, S., Thomasson, M., & Beswick, R. 2010, A&A, 513, A11
Osterbrock, D. E., & Martel, A. 1993, ApJ, 414, 552
Papadopoulos, P. P., van der Werf, P., Xilouris, E., Isaak, K. G., & Gao, Y. 2012a, ApJ, 751, 10
Papadopoulos, P. P., van der Werf, P. P., Xilouris, E. M., et al. 2012b, MNRAS, 426, 2601
Peeples, M. S., & Martini, P. 2006, ApJ, 652, 1097
Rampazzo, R., Marino, A., Tantalo, R., et al. 2007, MNRAS, 381, 245
Rampazzo, R., Plana, H., Longhetti, M., et al. 2003, MNRAS, 343, 819
Regan, M. W., Thornley, M. D., Helfer, T. T., et al. 2001, ApJ, 561, 218
Richter, O.-G., Sackett, P. D., & Sparke, L. S. 1994, AJ, 107, 99
Risaliti, G., Gilli, R., Maiolino, R., & Salvati, M. 2000, A&A, 357, 13
Risaliti, G., Maiolino, R., Marconi, A., et al. 2006, MNRAS, 365, 303
Robertson, B. E., & Bullock, J. S. 2008, ApJL, 685, L27
Rodríguez-Zaurín, J., Arribas, S., Monreal-Ibero, A., et al. 2011, A&A, 527, A60
Rothberg, B., & Fischer, J. 2010, ApJ, 712, 318
Rothberg, B., & Joseph, R. D. 2004, AJ, 128, 2098
Rothberg, B., & Joseph, R. D. 2006a, AJ, 131, 185
Rothberg, B., & Joseph, R. D. 2006b, AJ, 132, 976
Sakamoto, K., Aalto, S., Combes, F., Evans, A., & Peck, A. 2014, arXiv:1403.7117
Sakamoto, K., Ho, P. T. P., & Peck, A. B. 2006, ApJ, 644, 862
Sanders, D. B., & Mirabel, I. F. 1996, ARA&A, 34, 749
Sanders, D. B., Scoville, N. Z., & Soifer, B. T. 1991, ApJ, 370, 158
Schiminovich, D., van Gorkom, J. H., Dijkstra, M., et al. 2001, in ASP Conf. Ser. 240, Gas and Galaxy Evolution, ed. J. E. Hibbard, M. Rupen, & J. H. van Gorkom (San Francisco, CA: ASP), 864
Schiminovich, D., van Gorkom, J. H., & van der Hulst, J. M. 2013, AJ, 145, 34
Schombert, J. M., Wallin, J. F., & Struck-Marcell, C. 1990, AJ, 99, 497
Schweizer, F. 1982, ApJ, 252, 455
Schweizer, F. 1996, AJ, 111, 109
Schweizer, F., & Seitzer, P. 1992, AJ, 104, 1039
Schweizer, F., & Seitzer, P. 2007, AJ, 133, 2132
Schweizer, F., Seitzer, P., Kelson, D. D., Villanueva, E. V., & Walth, G. L. 2013, ApJ, 773, 148
Scoville, N. Z., Evans, A. S., Thompson, R., et al. 2000, AJ, 119, 991
Sekiguchi, K., & Wolstencroft, R. D. 1993, MNRAS, 263, 349
Shier, L. M., & Fischer, J. 1998, ApJ, 497, 163
Simien, F., & Prugniel, P. 1997, A&AS, 122, 521
Sliwa, K., Wilson, C. D., Petitpas, G. R., et al. 2012, ApJ, 753, 46
Smirnova, A., & Moiseev, A. 2010, MNRAS, 401, 307
Smith, B. J. 1991, ApJ, 378, 39
Smith, B. J. 1994, AJ, 107, 1695
Smith, D. A., Herter, T., Haynes, M. P., Beichman, C. A., & Gautier, T. N., III 1996, ApJS, 104, 217
Smith, E. P., & Hintzen, P. 1991, AJ, 101, 410
Soifer, B. T., Neugebauer, G., Matthews, K., et al. 2001, AJ, 122, 1213
Solomon, P. M., & Barrett, J. W. 1991, in IAU Symp. 146, Dynamics of Galaxies and Their Molecular Cloud Distributions, ed. F. Combes & F. Casoli (Cambridge: Cambridge Univ. Press), 235
Solomon, P. M., Downes, D., Radford, S. J. E., & Barrett, J. W. 1997, ApJ, 478, 144
Springel, V., & Hernquist, L. 2005, ApJL, 622, L9
Springob, C. M., Haynes, M. P., Giovanelli, R., & Kent, B. R. 2005, ApJS, 160, 149
Surace, J. A., Sanders, D. B., & Evans, A. S. 2000, ApJ, 529, 170
Tacconi, L. J., Neri, R., Genzel, R., et al. 2013, ApJ, 768, 74
Takeuchi, T. T., Buat, V., Heinis, S., et al. 2010, A&A, 514, A4
Taniguchi, Y., & Noguchi, M. 1991, AJ, 101, 1601
Taylor, G. B., Silver, C. S., Ulvestad, J. S., & Carilli, C. L. 1999, ApJ, 519, 185

Theureau, G., Bottinelli, L., Coudreau-Durand, N., et al. 1998, A&AS, 130, 333
Toomre, A. 1977, in The Evolution of Galaxies and Stellar Populations, ed. B. M. Tinsley & R. B. Larson (New Haven, CT: Yale Univ. Observatory), 401
van Driel, W., van den Broek, A. C., & de Jong, T. 1991, A&AS, 90, 55
Veilleux, S., Kim, D.-C., Sanders, D. B., Mazzarella, J. M., & Soifer, B. T. 1995, ApJS, 98, 171
Veilleux, S., Rupke, D. S. N., Kim, D.-C., et al. 2009, ApJS, 182, 628
Vlahakis, C., van der Werf, P., Israel, F. P., & Tilanus, R. P. J. 2013, MNRAS, 433, 1837
Wang, Z., Schweizer, F., & Scoville, N. Z. 1992, ApJ, 396, 510
Wang, Z., Scoville, N. Z., & Sanders, D. B. 1991, ApJ, 368, 112
Weistrop, D., Eggers, D., Hancock, M., et al. 2004, AJ, 127, 1360
Whitmore, B. C., Lucas, R. A., McElroy, D. B., et al. 1990, AJ, 100, 1489
Whitmore, B. C., Miller, B. W., Schweizer, F., & Fall, S. M. 1997, AJ, 114, 1797
Whitmore, B. C., Schweizer, F., Leitherer, C., Borne, K., & Robert, C. 1993, AJ, 106, 1354
Wiklind, T., Combes, F., & Henkel, C. 1995, A&A, 297, 643
Wilson, C. D., Petitpas, G. R., Iono, D., et al. 2008, ApJS, 178, 189
Wright, A., & Otrupcek, R. 1992, BICDS, 41, 47
Windhorst, R. A., Taylor, V. A., Jansen, R. A., et al. 2002, ApJS, 143, 113
Xu, C. K., Cao, C., Lu, N., et al. 2014, ApJ, 787, 48
Xu, X., Narayanan, D., & Walker, C. 2010, ApJL, 721, L112
Yamamura, I., Makiuti, S., Ikeda, N., et al. 2010, yCat, 2298, 0
Young, J. S., Xie, S., Tacconi, L., et al. 1995, ApJS, 98, 219
Yuan, T.-T., Kewley, L. J., & Sanders, D. B. 2010, ApJ, 709, 884
Zepf, S. E., Ashman, K. M., English, J., Freeman, K. C., & Sharples, R. M. 1999, AJ, 118, 752
Zhang, J. S., Henkel, C., Kadler, M., et al. 2006, A&A, 450, 933
Zhu, M., Seaquist, E. R., Davoust, E., Frayer, D. T., & Bushouse, H. A. 1999, AJ, 118, 145
Zhu, M., Seaquist, E. R., & Kuno, N. 2003, ApJ, 588, 243